Available online at www.sciencedirect.com
ScienceDirect
Comput. Methods Appl. Mech. Engrg. 278 (2014) 41–61
Computer methods in applied mechanics and engineering
www.elsevier.com/locate/cma

Statistical approach for a continuum description of damage evolution in soft collagenous tissues

Thomas Schmidt[a], Daniel Balzani[b,*], Gerhard A. Holzapfel[c]

[a] *Institute of Mechanics, Faculty of Engineering, University of Duisburg–Essen, 45141 Essen, Germany*
[b] *Dresden University of Technology, Faculty of Civil Engineering, 01069 Dresden, Germany*
[c] *Institute of Biomechanics, Graz University of Technology, 8010 Graz, Austria*

Received 26 April 2013; received in revised form 14 April 2014; accepted 20 April 2014
Available online 2 May 2014

Abstract

We propose a statistical approach to describe microscopic damage evolution in soft collagenous tissues such as arterial walls. The damage model extends a framework published by Balzani et al. (2012), Comput. Methods Appl. Mech. Engrg., 213–216:139–151, by postulating specific damage functions that result from the fibers' microstructure. Statistical distributions of three different microscopic quantities such as proteoglycan orientation, fibril length parameters and ultimate proteoglycan stretch are considered. The resulting stress–stretch response is compared with experimental data obtained from uniaxial tension tests given in the literature. In particular, the individual statistical distributions are analyzed in regard to their ability to capture the distinct softening hysteresis observed when subjecting soft tissues to cyclic loading in the supra-physiological domain. Details regarding the algorithmic implementation are provided, and the applicability of the model within a finite element framework is shown by simulating the overexpansion of simplified atherosclerotic arteries.

Keywords: Soft collagenous tissue; Microscopic damage; Proteoglycan; Statistical distribution; Strain energy; Atherosclerotic artery

1. Introduction

The mechanical behavior of soft collagenous tissues is a focus in current biomechanical research due to its significance onto the overall functioning of the cardiovascular system, in particular with a view to fatal consequences of diseased tissues such as heart attack, stroke and smoker's leg. For example, atherosclerotic degeneration may lead to arterial luminal narrowing, i.e. a stenosis. One possibility of a clinical treatment of such diseases is balloon angioplasty in combination with the insertion of a stent. Thereby a catheter is inflated to a pressure significantly higher than the blood pressure which induces damage at the fibrous level of the tissue. These supra-physiological situations need to be fully understood in order to reliably predict the outcome of such medical interventions, for example, to identify plaque ruptures. In this context computer simulations are expected to provide an important contribution.

To capture the mechanical behavior of arterial walls in the physiological loading domain various experiments have been carried out, see, for example, the reviews by Fung [1], Abé et al. [2], Humphrey [3] and Holzapfel and Ogden [4].

* Corresponding author. Tel.: +49 2011823603.
E-mail addresses: t.schmidt@uni-due.de (T. Schmidt), daniel.balzani@uni-due.de, daniel.balzani@tu-dresden.de (D. Balzani), holzapfel@tugraz.at (G.A. Holzapfel).

http://dx.doi.org/10.1016/j.cma.2014.04.011
0045-7825/

Within experimental studies Castaneda-Zuniga et al. [5] showed that supra-physiological loading conditions yield remanent deformations as soon as a certain load level is exceeded. This was confirmed by Oktay et al. [6] for carotid arteries of dogs, and by Holzapfel et al. [7] for human iliac arteries. Schulze-Bauer et al. [8] performed experiments of human adventitias under physiological and supra-physiological conditions and in particular the supra-physiological domain was analyzed in detail by Sommer et al. [9]. In the latter study it was found, by using cyclic tensile tests, that soft collagenous tissues show a complex stress-softening hysteresis. This has also been investigated in more detail by Weisbecker et al. [10] where a subsequent irreversible alignment of the collagen fibers turns out to be the reason for the softening.

Typically, the physiological behavior is described as hyperelastic and in this context the notion of polyconvex strain-energy functions is essential, see Ball [11]. In Holzapfel et al. [12] the first polyconvex model for soft biological tissues was introduced as an exponential function of the fourth (mixed) invariant of the structural tensor and the right Cauchy–Green tensor. Further polyconvex models to describe soft collagenous tissues were introduced by, for example, Itskov and Aksel [13], Balzani [14] and Ehret and Itskov [15]. These models are based on polyconvex functions for transverse isotropy and orthotropy, as suggested by Schröder and Neff [16]. In Balzani et al. [17] a general principle for the construction of anisotropic polyconvex functions which automatically fulfill the condition of a stress-free reference configuration was provided.

For the description of the stress-softening behavior, as observed under supra-physiological conditions, as a result of microscopic tissue damage, the framework of continuum damage mechanics was often considered. In this context the first works mainly deal with the modeling of the Mullins effect in rubber or polymers at large strains, see, for example, Simo [18], Govindjee and Simo [19] and Miehe [20], which was later extended to a saturation behavior, see Miehe and Keck [21]. In Dargazany and Itskov [22] the authors model anisotropic damage in carbon black filled rubbers based on changes in the inter-aggregate distribution of polymer chains and thus avoid the use of a phenomenological damage function.

An alternative phenomenological approach is to model damage as pseudo-elasticity, see, for example, Ogden and Roxburgh [23,24] and Dorfmann and Ogden [25]. In Gracia et al. [26] the Ogden and Roxburgh model was compared to a continuum damage mechanics model by Simo in terms of its capability to describe the Mullins effect in industrial rubber components. In Weisbecker et al. [10] the approach was used for the description of damage in soft collagenous tissues. A further alternative was provided by considering relaxed incremental variational formulations, see, for example, Francfort and Marigo [27], Francfort and Garroni [28] and Gürses and Miehe [29] for small strains. In Balzani and Ortiz [30] an extension to large strains was given for fiber-reinforced materials.

For the description of anisotropic damage in soft collagenous tissues using scalar-valued variables instead of damage tensors a phenomenological approach is given by Balzani et al. [31]. In Gasser and Holzapfel [32] the framework of finite plasticity was used to describe remanent strains due to overstretch. Hereby, remaining deformations of the fibers were assumed. Based on continuum damage mechanics remanent deformations in the fibers were also taken into account by Ehret and Itskov [33]. In Balzani et al. [34] a principle was provided for the construction of damage models that account for remanent strains after unloading, and which still guarantee polyconvexity in the undamaged (physiological) domain. Thereby specific functions were derived and a good correlation with experimental data was obtained. Damage of the matrix material was, for example, taken into account by Calvo et al. [35] and Natali et al. [36]. Sáez et al. [37] introduced a one-dimensional damage variable in the fiber direction and considered a statistical distribution of fibers. In Peña [38] several scalar-valued damage functions for soft biological tissues available in the literature were compared and also a new model was introduced.

Although some of the parameters in the above-mentioned damage models provide to some extent a micromechanical interpretation they incorporated damage by defining suitable phenomenological damage functions. A first model taking into account a stochastically distributed waviness and a subsequent rupture of the individual fibers as the main driving force for damage evolution was given by Rodríguez et al. [39]. However, damage appears to occur at an even lower length scale than the fiber level. Collagen fibers are composed of a complex hierarchical microstructure consisting of fibrils interconnected by proteoglycans (PGs). Subsequently, the associated length scale at this fibril level is referred to as microscale. In, for example, Scott [40] it was reported that there is a remanent sliding of the PGs when exceeding a characteristic PG stretch which can be assumed to be a main contributor to the remanent sliding observed at the macroscale. Therefore, a statistical distribution of parameters characterizing the fibril level can be expected to be responsible for the damage evolution. That is why in the present study stochastic distributions of several microscopic quantities are considered, based on a simple fiber unit-cell; the resulting damage evolution is analyzed.

The paper is organized as follows: Section 2 first provides a brief introduction into the continuum mechanical constitutive framework. Then the new damage approach is introduced and different statistically distributed quantities at the fibril level are considered. Furthermore, details regarding the algorithmic implementation are given. In Section 3 the capability of the resulting specific models to reproduce the mechanical behavior of overstretched tissues is shown by adjusting the model parameters to experimental data. Section 4 documents representative numerical examples within a finite element framework. The distribution of damage after circumferential overstretches of simplified atherosclerotic arteries is investigated. Section 5 concludes the paper.

2. Mechanical modeling

2.1. Framework for damage modeling

The body of interest is denoted by $\mathcal{B} \subset \mathbb{R}^3$ in the (undeformed) reference configuration and parameterized by $\boldsymbol{X}$. In the (deformed) current configuration it is denoted by $\mathcal{S} \subset \mathbb{R}^3$ and parameterized by $\boldsymbol{x}$. The motion $\varphi_t : \mathcal{B} \to \mathcal{S}$ at time $t \in \mathbb{R}_+$ maps points $\boldsymbol{X} \in \mathcal{B}$ onto points $\boldsymbol{x} \in \mathcal{S}$. The deformation gradient $\boldsymbol{F}$ and the right Cauchy–Green tensor $\boldsymbol{C}$ are given by $\boldsymbol{F}(\boldsymbol{X}) := \nabla\varphi_t(\boldsymbol{X})$ and $\boldsymbol{C} := \boldsymbol{F}^T\boldsymbol{F}$, with the Jacobian $J := \det\boldsymbol{F} > 0$. For hyperelastic materials the existence of a strain–energy function $\Psi := \Psi(\boldsymbol{C})$, defined per unit reference volume, is postulated and the second Piola–Kirchhoff stress tensor is calculated by $\boldsymbol{S} = 2\partial_{\boldsymbol{C}}\Psi$. The physical Cauchy stress tensor can then be computed as $\boldsymbol{\sigma} = J^{-1}\boldsymbol{F}\boldsymbol{S}\boldsymbol{F}^T$. Anisotropic materials can be described within the concept of structural tensors, see, for example, Spencer [41], Boehler [42], or Zheng and Spencer [43]. For the case of fiber-reinforced materials, with the assumption that the individual fiber families have no interaction to each other, superimposed transversely isotropic strain–energy functions can be considered, and the structural tensor of each fiber family is given by

$$\boldsymbol{M}_{(a)} := \boldsymbol{A}_{(a)} \otimes \boldsymbol{A}_{(a)} \quad \text{with } a = 1, \ldots, n_a, \tag{1}$$

where n_a denotes the number of different fiber directions. Hence, the invariants of the deformation gradient and the structural tensor have to be considered as

$$I_1 := \mathrm{tr}\boldsymbol{C}, \qquad I_2 := \mathrm{tr}[\mathrm{Cof}\boldsymbol{C}], \qquad I_3 := \det\boldsymbol{C}, \qquad J_4^{(a)} := \mathrm{tr}[\boldsymbol{C}\boldsymbol{M}_{(a)}], \qquad J_5^{(a)} := \mathrm{tr}[\boldsymbol{C}^2\boldsymbol{M}_{(a)}], \tag{2}$$

where $\mathrm{Cof}[\boldsymbol{C}] = \det[\boldsymbol{C}]\boldsymbol{C}^{-1}$. Note that the fifth invariant $J_5^{(a)}$ is not polyconvex. Alternatively, the polyconvex functions, as introduced by Schröder and Neff [16], i.e.

$$K_1^{(a)} := \mathrm{tr}[\mathrm{Cof}\boldsymbol{C}\boldsymbol{M}_{(a)}] = J_5^{(a)} - I_1 J_4^{(a)} + I_2, \tag{3}$$

$$K_2^{(a)} := \mathrm{tr}[\boldsymbol{C}(\boldsymbol{I} - \boldsymbol{M}_{(a)})] = I_1 - J_4^{(a)}, \tag{4}$$

$$K_3^{(a)} := \mathrm{tr}[\mathrm{Cof}\boldsymbol{C}(\boldsymbol{I} - \boldsymbol{M}_{(a)})] = I_1 J_4^{(a)} - J_5^{(a)}, \tag{5}$$

can be used when constructing the strain–energy function. To describe a soft collagenous tissue the typical additive decomposition

$$\Psi = \Psi^{\mathrm{pen}}(\det\boldsymbol{C}) + \Psi^{\mathrm{iso}}(\boldsymbol{C}) + \sum_{a=1}^{n_a} \Psi_{(a)}^{\mathrm{ti}}(\boldsymbol{C}, \boldsymbol{M}_{(a)}) \tag{6}$$

is considered (Holzapfel et al. [12]), wherein the isotropic part is defined as

$$\Psi^{\mathrm{iso}} = c_1 \left(\frac{I_1}{I_3^{1/3}} - 3 \right), \tag{7}$$

with the stress-like parameter $c_1 > 0$ representing the ground substance, i.e. the matrix material. The transversely isotropic part $\Psi_{(a)}^{\mathrm{ti}}$ represents the energy stored in the fiber family a. The function Ψ^{pen} is a penalty term to enforce incompressibility. The constitutive framework proposed in Balzani et al. [34], see also [31], is used. Therein, remanent strains in the physiological loading domain after supra-physiological loading can be described. Moreover, the polyconvexity condition is satisfied in the physiological (undamaged) domain. A one-dimensional damage variable $D_{(a)} \in [0, 1]$ is incorporated into each of the fiber energies according to

$$\Psi^{\mathrm{ti}}_{(a)} := m[P_{(a)}(\boldsymbol{C}, D_{(a)})] \quad \text{with } P_{(a)} = (1 - D_{(a)})\,\Psi^{\mathrm{ti},0}_{(a)} - c. \tag{8}$$

Herein, the $(1 - D_{(a)})$-approach is embedded in an internal function $P_{(a)}$. The parameter c is equal to the value of the effective transversely isotropic function $\Psi^{\mathrm{ti},0}_{(a)}$ in the reference configuration. To describe the fiber energy, polyconvex functions such as J_4 or K_3 can be used. The external function $m[P(X)]$ needs to be convex and monotonically increasing. In more detail the two functions $m[(\bullet)] = \frac{k_1}{2k_2}[\exp(k_2\langle(\bullet)\rangle^2) - 1]$ and $m[(\bullet)] = \alpha_1\langle(\bullet)\rangle^{\alpha_2}$ are considered to characterize the stiffening of the fiber response. Therein, k_1 and α_1 are stress-like parameters, whereas k_2 and α_2 are dimensionless. The use of the Macaulay brackets $\langle(\bullet)\rangle = \frac{1}{2}[(\bullet) + |(\bullet)|]$ filters out positive values. The resulting second Piola–Kirchhoff stress tensor reads

$$\boldsymbol{S} = 2\frac{\partial\,\Psi}{\partial\boldsymbol{C}} = \boldsymbol{S}^{\mathrm{pen}} + \boldsymbol{S}^{\mathrm{iso}} + \sum_{a=1}^{n_a}\boldsymbol{S}^{\mathrm{ti}}_{(a)}, \quad \text{with } \boldsymbol{S}^{\mathrm{pen}} = 2\frac{\partial\,\Psi^{\mathrm{pen}}}{\partial\boldsymbol{C}},\ \boldsymbol{S}^{\mathrm{iso}} = 2\frac{\partial\,\Psi^{\mathrm{iso}}}{\partial\boldsymbol{C}}, \tag{9}$$

and the transversely isotropic part

$$\boldsymbol{S}^{\mathrm{ti}}_{(a)} = (1 - D_{(a)})\boldsymbol{S}^{\mathrm{ti},0}_{(a)} \quad \text{with } \boldsymbol{S}^{\mathrm{ti},0}_{(a)} = 2m'\frac{\partial\,\Psi^{\mathrm{ti},0}_{(a)}}{\partial\boldsymbol{C}}. \tag{10}$$

Hereby, m' denotes the partial derivative $\partial_P m$. The main problem with respect to specific model formulations is of course the definition of a suitable effective function $\Psi^{\mathrm{ti},0}_{(a)}$ and the damage variable $D_{(a)}$. Whereas for the effective function describing the physiological behavior some micromechanically motivated formulations are given in the literature, see, for example, [12,17], there are no damage functions available that are directly derived from microscopic findings. Therefore, the main focus in the next section is to construct suitable damage formulations that are indeed based on micromechanical quantities.

2.2. Micromechanically motivated damage function

In contrast to Balzani et al. [34], where a phenomenological function for D has been used, in this work a micromechanically based stretch-induced damage function is introduced. This has the advantage that the parameters of the function allow for a physical interpretation and, thus, may in principle be measurable. The evolution of microscopic damage is assumed to be a result of a subsequent loss of connectivity of the interfibrillar proteoglycan (PG) bridges induced by statistically distributed microstructure quantities. This approach is based on a sliding filament model, see the review article by Scott [40], which states the capability of PG bridges to store reversible stretches only in a certain domain. This is due to their composition of two neighboring anionic glycosaminoglycan (AGAG) chains, which can bond differently, and thus enable sliding of the collagen fibrils relative to each other, if a stress is applied; see also Gasser [44].

Therefore, a simplified fibril unit-cell, as shown in Fig. 1(a), is considered, which consists of two half collagen fibrils that are interconnected by PG bridges. The orientation of the individual PG bridges is described by the initial PG angle α, which is dispersed at the microscale, cf. Fig. 1(b) taken from Liao and Vesely [45]. The initial transverse distance, the length of the fibrils and the initial overlap of two fibrils are given by d_0, L_{cf} and L_{ov}, respectively. Depending on a macroscopic fiber stretch, denoted by λ_{fib}, the fibrils extend relatively to each other and so do the PG bridges. For this microscopic model a uniaxial isochoric extension of the fiber is assumed, so that the fiber stretch in the transverse direction is $1/\sqrt{\lambda_{\mathrm{fib}}}$, and the transverse distance d of the collagen fibrils in the current configuration is

$$d = \frac{d_0}{\sqrt{\lambda_{\mathrm{fib}}}}. \tag{11}$$

The fiber stretch in terms of the fourth invariant is according to Eq. $(2)_4$, i.e. $\lambda_{\mathrm{fib}} = \sqrt{J_4}$. This yields a relative displacement $u = (\lambda_{\mathrm{fib}} - 1)(L_{\mathrm{cf}} - L_{\mathrm{ov}})$ of the collagen fibrils.

The stretch of a PG bridge, say λ_{pg}, can be derived with the help of standard trigonometric arguments, as the ratio of lengths in the current (L_{pg}) and the reference ($L_{\mathrm{pg},0}$) configuration, i.e.

$$\lambda_{\mathrm{pg}} = \frac{L_{\mathrm{pg}}}{L_{\mathrm{pg},0}} = \sqrt{[\cos\alpha - L(\lambda_{\mathrm{fib}} - 1)\sin\alpha]^2 + \frac{\sin^2\alpha}{\lambda_{\mathrm{fib}}}}, \tag{12}$$

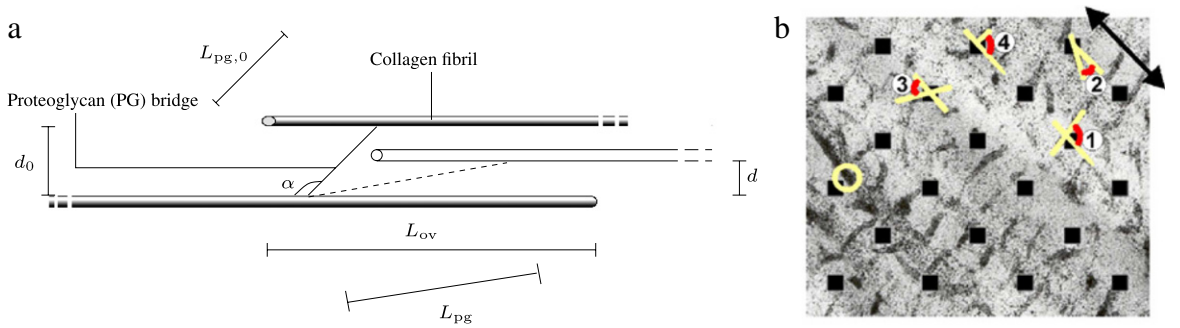

Fig. 1. (a) Geometrical quantities defining the fibril–proteoglycan microstructure in the reference and current configuration; (b) transmission electron microscopy image showing measurements of four different PG skewness angles $\theta = |\alpha - \pi/2|$ in porcine mitral valve chordae, taken from Liao and Vesely [45]. The arrow shows the orientation of collagen fibrils. It can be observed, that the skewness angles are subject to large variations.

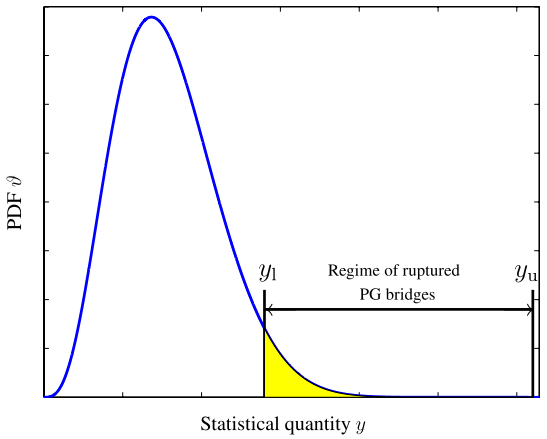

Fig. 2. Evaluation of the damage variable D by integrating the related probability density function (PDF) ϑ over the lower and upper bounds y_{l} and y_{u}, respectively; compare with Eq. (15).

whereby the dimensionless internal length parameter

$$L = \frac{L_{\mathrm{cf}} - L_{\mathrm{ov}}}{d_0} \tag{13}$$

has been introduced. The statement by Scott [40], that PG stretch is reversible as long as the overlap between two AGAG chains is above a critical value, motivates the introduction of a parameter $\lambda_{\mathrm{pg}}^{\mathrm{sust}}$ to describe the maximum *sust*ainable PG stretch. The quantities α and L, which are microstructural properties of the collagen fibers influencing the PG stretch (12), and the ultimate PG stretch $\lambda_{\mathrm{pg}}^{\mathrm{sust}}$, may be assumed to be statistically distributed. Here, we focus on three different cases where each case is based on a statistical distribution of one of these microstructural quantities (α, L and $\lambda_{\mathrm{pg}}^{\mathrm{sust}}$), the others are then assumed to be deterministic. This enables an analytical calculation of the domain of ruptured PG bridges characterized by $\lambda_{\mathrm{pg}} - \lambda_{\mathrm{pg}}^{\mathrm{sust}} \geq 0$. Depending on the statistically distributed quantity denoted by $y \in (y_{\min}, y_{\max})$, the lower bound y_{l}, the upper bound y_{u} or both are solutions of the equation

$$\lambda_{\mathrm{pg}} - \lambda_{\mathrm{pg}}^{\mathrm{sust}} = 0. \tag{14}$$

The damage variable $D := D(\lambda_{\mathrm{fib}}) \in [0, 1]$ is then defined as the amount of ruptured PG bridges, and thus evaluated by integrating the related probability density function (PDF) ϑ of the respective quantity over y_{l} and y_{u} (cf. Fig. 2).

$$D(\lambda_{\mathrm{fib}}) = \int_{y_{\mathrm{l}}(\lambda_{\mathrm{fib}})}^{y_{\mathrm{u}}(\lambda_{\mathrm{fib}})} \vartheta(y)\mathrm{d}y = \hat{\vartheta}(y_{\mathrm{u}}) - \hat{\vartheta}(y_{\mathrm{l}}) \quad \text{with} \int_{y} \vartheta(y)\mathrm{d}y = 1, \tag{15}$$

where $\hat{\vartheta}$ denotes the antiderivative of the related PDF and thus the cumulative distribution function (CDF). Note that if a joint probability distribution depending on all three parameters (α, L and $\lambda_{\mathrm{pg}}^{\mathrm{sust}}$) was considered, the solution of

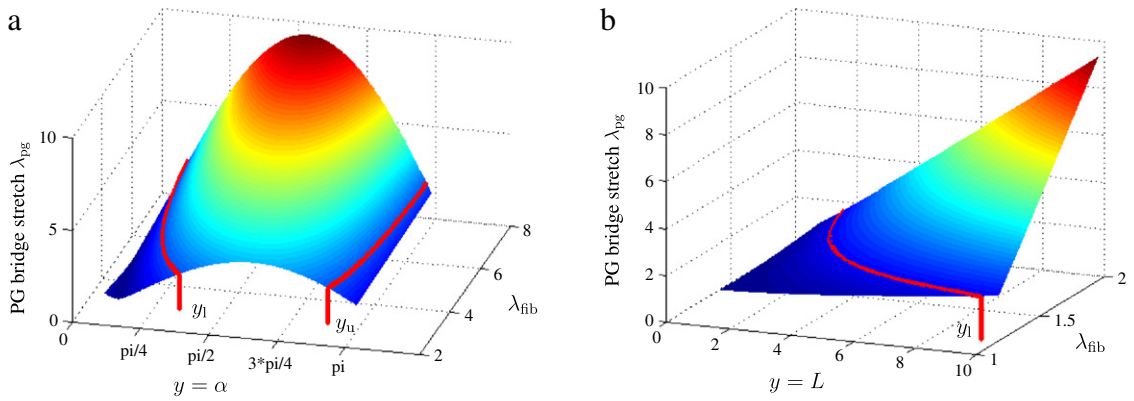

Fig. 3. Lower and upper bounds (y_l, y_u) for a domain of ruptured PG bridges under consideration of (a) a statistically distributed PG angle α, and (b) a statistically distributed internal length parameter L, respectively.

(14) would yield a complicated expression and thereby the analytical or even numerical calculation of $(15)_1$ would be complex. The damage variable D is thereby naturally restricted to the domain $0 \leq D \leq 1$. In the following the Gaussian distribution, say $\hat{\vartheta}_{\text{Gauss}}$, and the beta distribution, say $\hat{\vartheta}_{\text{beta}}$, are taken into account for the respective quantities. Hence, the CDFs are

$$\hat{\vartheta}_{\text{Gauss}}(y) = \frac{1}{2} + \frac{1}{\sqrt{\pi}} \int_0^{\frac{y-\mu}{\sqrt{2}\sigma_D}} e^{-\tilde{y}^2} \mathrm{d}\tilde{y}, \tag{16}$$

$$\hat{\vartheta}_{\text{beta}}(y) = \frac{1}{B(a,b)} \int_0^{y} \tilde{y}^{a-1}(1-\tilde{y})^{b-1} \mathrm{d}\tilde{y} \quad \text{with } 0 < y < 1, \tag{17}$$

where μ and σ_D denote the mean value and the standard deviation of the Gaussian distribution, respectively. The beta distribution is characterized by two shape parameters a and b, and the beta function B.

2.2.1. Statistical distribution of the proteoglycan orientation

We interpret the initial PG angle α as a statistically distributed quantity, i.e. $y = \alpha \in]0, \pi[$. In addition, since α is located within an interval with well-defined bounds, it seems reasonable to take into account a beta distribution, which is defined on the open interval]0, 1[. Thus, the domain can be simply scaled by the factor π so that we obtain

$$\hat{\vartheta}_{\text{beta}}(\alpha) = \frac{1}{\pi\, B(a,b)} \int_0^{\alpha} \left(\frac{\tilde{\alpha}}{\pi}\right)^{a-1} \left(1 - \frac{\tilde{\alpha}}{\pi}\right)^{b-1} \mathrm{d}\tilde{\alpha} \quad \text{with } 0 < \alpha < \pi. \tag{18}$$

In contrast to the beta distribution a Gaussian distribution may yield an error since $\hat{\vartheta}_{\text{Gauss}}$ is defined on an infinite domain, and unreasonable values of the distribution may be obtained depending on μ and σ_D; therefore, a Gaussian distribution was not considered. The evaluation of (14) with respect to α yields either no or two real solutions, see Fig. 3(a). If no real solution is obtained it means that none of the PGs is stretched such that the ultimate stretch is exceeded. In the case of two positive real solutions, these are defined as the bounds y_l and y_u of the domain of ruptured PG bridges, i.e.

$$y_l = \alpha_l = \arctan\left(a_{16}, \frac{a_{20} + a_4 a_7 - L^2 \lambda_{\text{fib}} a_7 - a_7}{a_{16} a_{19}}\right), \tag{19}$$

$$y_u = \alpha_u = \arctan\left(a_{17}, \frac{a_{20} - a_4 a_{14} + L^2 \lambda_{\text{fib}} a_{14} + a_{14}}{a_{17} a_{19}}\right), \tag{20}$$

with the abbreviations $a_1, \ldots, a_{20}$, as listed in the Appendix A, and the two-argument function $\arctan(x, y) = -i \ln[(x+iy)(x^2+y^2)^{-1/2}]$. The microscopical images presented in, for example, Dingemans et al. [46] and Liao and Vesely [45] motivate the consideration of statistically distributed PG orientations. However, the distribution seems to

be restricted to a domain close to the perpendicular case. As it is shown in Section 3, the consideration of a statistically distributed PG orientation with a rather moderate variation still yields a pronounced softening hysteresis.

2.2.2. Statistical distribution of the internal length parameter

Although the incorporation of a statistically distributed PG orientation appears to be reasonable, the statistical distribution of different microscopic quantities may be dominant for the damage evolution. Therefore, a further quantity, the internal length $L \in \,]0, +\infty]$, is assumed to be statistically distributed. In this case a lower bound y_l of a domain of ruptured PG bridges can be evaluated as

$$y_\mathrm{l} = L_\mathrm{l} = \frac{\cos\alpha + \sqrt{\lambda_\mathrm{pg}^{\mathrm{sust}2} - \frac{\sin^2\alpha}{\lambda_\mathrm{fib}}}}{(\lambda_\mathrm{fib} - 1)\sin\alpha} \quad \text{with } 0 < \alpha < \pi, \tag{21}$$

which is the relevant solution of (14), see Fig. 3(b). Since the domain size of the statistical distribution is not yet known, a Gaussian distribution is taken into account here. For the distribution of L there is no physically relevant upper bound associated to a limit of the domain of ruptured PG bridges, and thus $\hat{\vartheta}(y_\mathrm{u})$ in (15) is set to unity, i.e.

$$D = 1 - \hat{\vartheta}(y_\mathrm{l}). \tag{22}$$

2.2.3. Statistical distribution of the ultimate proteoglycan stretch

By considering the ultimate PG stretch $\lambda_\mathrm{pg}^{\mathrm{sust}}$ to be statistically distributed the upper bound y_u of the domain of ruptured PG bridges is equal to the maximally reached PG stretch (12) over the load history, i.e.

$$y_\mathrm{u} = \sqrt{[\cos\alpha - L(\lambda_\mathrm{fib} - 1)\sin\alpha]^2 + \frac{\sin^2\alpha}{\lambda_\mathrm{fib}}}, \tag{23}$$

because all PG bridges with $\lambda_\mathrm{pg}^{\mathrm{sust}}$ smaller than the maximally reached PG stretch are ruptured. The antiderivative $\hat{\vartheta}(y_\mathrm{l})$ evaluated at the lower bound in (15) is, therefore, set to zero such that the damage variable D is simply given by

$$D = \hat{\vartheta}(y_\mathrm{u}). \tag{24}$$

The minimum and maximum values of the distribution of the ultimate PG stretch are clearly defined. For the minimum value the unstretched case $\lambda_{\mathrm{pg,min}}^{\mathrm{sust}} = 1$ is taken into account. As soon as the AGAG chains are pulled apart twice their length, there is no more overlap of the AGAG chains, when assuming that they do not store reversible stretches themselves. Thus, the maximum value is given by the maximal stretch bearable by a PG bridge which is $\lambda_{\mathrm{pg,max}}^{\mathrm{sust}} = 2$. Note that even lower maximum values may be physically possible, however, there is no experimental evidence. Thus, beta distributions are taken into account with the open interval $1 < \lambda_\mathrm{pg}^{\mathrm{sust}} < 2$. Due to this shift of the range of the random variable we consider $D = \hat{\vartheta}(y_\mathrm{u} - 1)$.

2.3. Thermodynamic consistency

For the proof of thermodynamic consistency the Clausius–Duhem inequality needs to be analyzed. Therefore, the derivative of the strain energy (6) is computed as

$$\dot{\Psi} = \frac{\partial \Psi}{\partial \boldsymbol{C}} : \dot{\boldsymbol{C}} + \sum_a \frac{\partial \Psi}{\partial D_{(a)}} \dot{D}_{(a)} = \frac{\partial \Psi}{\partial \boldsymbol{C}} : \dot{\boldsymbol{C}} - \sum_a \frac{\partial m}{\partial P_{(a)}} \Psi_{(a)}^{\mathrm{ti},0} \dot{D}_{(a)}. \tag{25}$$

Insertion into the Clausius–Duhem inequality for isothermal conditions yields

$$\mathcal{D} = \left(\frac{1}{2}\boldsymbol{S} - \frac{\partial \Psi}{\partial \boldsymbol{C}}\right) : \dot{\boldsymbol{C}} + \sum_a m' \Psi_{(a)}^{\mathrm{ti},0} \dot{D}_{(a)} \geq 0, \tag{26}$$

with the abbreviation $m' := \partial_{P_{(a)}} m$. Following the standard argument of rational continuum mechanics the Clausius–Duhem inequality has to be satisfied for arbitrary mechanical states. Setting the standard constitutive equation for the

second Piola–Kirchhoff stresses as in $(9)_1$, the dissipation $\mathcal{D}_{\text{red}}$ reduces to

$$\mathcal{D}_{\text{red}} := \sum_a m' \, \Psi^{\text{ti},0}_{(a)} \dot{D}_{(a)} \geq 0. \tag{27}$$

Since monotonically increasing functions m ($m' > 0$) are chosen and the considered transversely isotropic energy functions are always positive or zero due to the Macaulay bracket ($\Psi^{\text{ti},0}_{(a)} \geq 0$), the rate $\dot{D}_{(a)}$ of the damage variable has to be greater than or equal to zero. Considering $(15)_1$, $\dot{D}_{(a)} \geq 0$ can only be achieved for

$$\dot{y}_l \leq 0 \quad \text{and} \quad \dot{y}_u \geq 0. \tag{28}$$

The relations (28) represent the physical constraint that the regime of failed PG bridges cannot decrease during load history, which is also in line with the micromechanical considerations. The latter condition is enforced by means of trial values within the algorithmic treatment, see Section 2.4.

2.4. Algorithmic implementation

For an implementation into a finite element framework the linearization of the stress tensor is required. With respect to the structure of (9) the increment Δ of the second Piola–Kirchhoff stress tensor $\boldsymbol{S}$ is obtained as

$$\Delta \boldsymbol{S}(\boldsymbol{C}, D_{(a)}) = \frac{\partial \boldsymbol{S}^{\text{pen}}}{\partial \boldsymbol{C}} : \Delta \boldsymbol{C} + \frac{\partial \boldsymbol{S}^{\text{iso}}}{\partial \boldsymbol{C}} : \Delta \boldsymbol{C} + \sum_{a=1}^{2} \left(\frac{\partial \boldsymbol{S}^{\text{ti}}_{(a)}}{\partial \boldsymbol{C}} : \Delta \boldsymbol{C} + \frac{\partial \boldsymbol{S}^{\text{ti}}_{(a)}}{\partial D_{(a)}} \Delta D_{(a)} \right), \tag{29}$$

with the derivatives

$$\frac{\partial \boldsymbol{S}^{\text{ti}}_{(a)}}{\partial D_{(a)}} = -\boldsymbol{S}^{\text{ti},0}_{(a)} \quad \text{and} \quad \Delta D_{(a)} = \frac{\partial D_{(a)}}{\partial \lambda^{(a)}_{\text{fib}}} \Delta \lambda^{(a)}_{\text{fib}}, \tag{30}$$

where $(10)_1$ and (15) have been used. By using the increment Δ of $\lambda^{(a)}_{\text{fib}}$ we get

$$\Delta D_{(a)} = \frac{\partial D_{(a)}}{\partial \lambda^{(a)}_{\text{fib}}} \frac{\partial \lambda^{(a)}_{\text{fib}}}{\partial \boldsymbol{C}} : \Delta \boldsymbol{C}. \tag{31}$$

By inserting these relations and $(10)_2$ into (29) the incremental stress–strain relation can be written as

$$\Delta \boldsymbol{S} = \mathbb{C} : \frac{1}{2} \Delta \boldsymbol{C}, \tag{32}$$

wherein the elasticity tensor in the material description can be decoupled as

$$\mathbb{C} = \mathbb{C}^{\text{elas}} + \sum_{a=1}^{2} \mathbb{C}^{\text{ti}}_{(a)} \quad \text{with } \mathbb{C}^{\text{ti}}_{(a)} = \mathbb{C}^{\text{e}D}_{(a)} + \mathbb{C}^{D}_{(a)}. \tag{33}$$

Herein, the part $\mathbb{C}^{\text{elas}}$ can be identified as the (standard) isotropic elasticity tensor for hyperelasticity, i.e. (Holzapfel [47])

$$\mathbb{C}^{\text{elas}} = \mathbb{C}^{\text{pen}} + \mathbb{C}^{\text{iso}} = 4 \frac{\partial^2 \Psi^{\text{pen}}}{\partial \boldsymbol{C} \partial \boldsymbol{C}} + 4 \frac{\partial^2 \Psi^{\text{iso}}}{\partial \boldsymbol{C} \partial \boldsymbol{C}}. \tag{34}$$

The part $\mathbb{C}^{\text{e}D}_{(a)}$ is identified as the transversely isotropic elasticity tensor related to damage, i.e.

$$\mathbb{C}^{\text{e}D}_{(a)} = (1 - D_{(a)}) \mathbb{C}^{\text{ti},0}_{(a)} + 4(1 - D_{(a)})^2 m'' \frac{\partial \Psi^{\text{ti},0}_{(a)}}{\partial \boldsymbol{C}} \otimes \frac{\partial \Psi^{\text{ti},0}_{(a)}}{\partial \boldsymbol{C}}, \tag{35}$$

Table 1
Algorithmic box for the computation of the stress and elasticity tensors. The initial values of the history variables at $k = 0$ are set to ${}^0y_{\mathrm{l}} = y_{\max}$, ${}^0y_{\mathrm{u}} = y_{\min}$, ${}^0D_{(a)} = 0$. Depending on the specific random variable it may occur that there is only an upper or lower bound and thus the if-conditions 'and/or' should be considered appropriately.

(I) Compute $\boldsymbol{S}^{\mathrm{pen}}$, $\boldsymbol{S}^{\mathrm{iso}}$, $\mathbb{C}^{\mathrm{pen}}$ and $\mathbb{C}^{\mathrm{iso}}$
(II) Do for $a = 1, 2$
  (i) Compute fiber stretch $\lambda_{\mathrm{fib}}^{(a)}$
  (ii) Read history (${}^k y_{\mathrm{l}}^{(a)}$ and/or ${}^k y_{\mathrm{u}}^{(a)}$) and compute bounds ($y_{\mathrm{l}}^{(a)}$ and/or $y_{\mathrm{u}}^{(a)}$)
  (iii) if $y_{\mathrm{l}}^{(a)}$ and/or $y_{\mathrm{u}}^{(a)}$ is complex or ($y_{\mathrm{l}}^{(a)} > {}^k y_{\mathrm{l}}^{(a)}$ and/or $y_{\mathrm{u}}^{(a)} < {}^k y_{\mathrm{u}}^{(a)}$) then set from history $y_{\mathrm{l}}^{(a)} = {}^k y_{\mathrm{l}}^{(a)}$ and/or $y_{\mathrm{u}}^{(a)} = {}^k y_{\mathrm{u}}^{(a)}$
  (iv) if $y_{\mathrm{l}}^{(a)} < {}^0 y_{\mathrm{l}}^{(a)}$ and/or $y_{\mathrm{u}}^{(a)} > {}^0 y_{\mathrm{u}}^{(a)}$ then compute damage function $D_{(a)} = \hat{\vartheta}(y_{\mathrm{u}}^{(a)}) - \hat{\vartheta}(y_{\mathrm{l}}^{(a)})$
  (v) Compute transversely isotropic stress and elasticity tensors
    (a) Stress tensor $\boldsymbol{S}_{(a)}^{\mathrm{ti}} = \left(1 - D_{(a)}\right) \boldsymbol{S}_{(a)}^{\mathrm{ti},0}$
    (b) Elasticity tensor (see Table 2)
(III) Compute total stress and elasticity tensors

$$\boldsymbol{S} = \boldsymbol{S}^{\mathrm{pen}} + \boldsymbol{S}^{\mathrm{iso}} + \sum_{a=1}^{2} \boldsymbol{S}_{(a)}^{\mathrm{ti}} \quad \text{and} \quad \mathbb{C} = \mathbb{C}^{\mathrm{pen}} + \mathbb{C}^{\mathrm{iso}} + \sum_{a=1}^{2} \mathbb{C}_{(a)}^{\mathrm{ti}}$$

Table 2
Algorithmic box for the computation of the transversely isotropic elasticity tensor.

(i) Compute effective elasticity tensor $\mathbb{C}_{(a)}^{\mathrm{ti},0} = 4m' \partial^2_{\boldsymbol{C}\boldsymbol{C}} \Psi_{(a)}^{\mathrm{ti},0}$
(ii) Compute parts of the transversely isotropic elasticity tensor
- $\mathbb{C}_{(a)}^{\mathrm{ti}} := \mathbb{C}_{(a)}^{\mathrm{e}D} = \left(1 - D_{(a)}\right) \mathbb{C}_{(a)}^{\mathrm{ti},0} + 4m''(1 - D_{(a)})^2 \frac{\partial \psi_{(a)}^{\mathrm{ti},0}}{\partial \boldsymbol{C}} \otimes \frac{\partial \psi_{(a)}^{\mathrm{ti},0}}{\partial \boldsymbol{C}}$
- if ($y_{\mathrm{l}}^{(a)}$ and/or $y_{\mathrm{u}}^{(a)}$) is real and ($y_{\mathrm{l}}^{(a)} < {}^k y_{\mathrm{l}}^{(a)}$ and/or $y_{\mathrm{u}}^{(a)} > {}^k y_{\mathrm{u}}^{(a)}$) then

$$\mathbb{C}_{(a)}^{D} = -4 \left[m' + m''(1 - D_{(a)}) \Psi_{(a)}^{\mathrm{ti},0} \right] \frac{\partial D_{(a)}}{\partial \lambda_{\mathrm{fib}}^{(a)}} \frac{\partial \psi_{(a)}^{\mathrm{ti},0}}{\partial \boldsymbol{C}} \otimes \frac{\partial \lambda_{\mathrm{fib}}^{(a)}}{\partial \boldsymbol{C}}$$

$$\mathbb{C}_{(a)}^{\mathrm{ti}} \Leftarrow \mathbb{C}_{(a)}^{\mathrm{ti}} + \mathbb{C}_{(a)}^{D}$$

cf. [34], with the abbreviation $m'' := \partial^2_{PP} m$ and $\mathbb{C}_{(a)}^{\mathrm{ti},0} = 4m' \partial^2_{CC} \Psi_{(a)}^{\mathrm{ti},0}$. Note that $\mathbb{C}_{(a)}^{\mathrm{ti},0}$ is not identical to the elasticity tensor of the undamaged transversely isotropic strain–energy function. The damage evolution part $\mathbb{C}_{(a)}^{D}$ is given by

$$\mathbb{C}_{(a)}^{D} = \begin{cases} -4 \left[m' + m''(1 - D_{(a)}) \Psi_{(a)}^{\mathrm{ti},0} \right] \dfrac{\partial D_{(a)}}{\partial \lambda_{\mathrm{fib}}^{(a)}} \dfrac{\partial \Psi_{(a)}^{\mathrm{ti},0}}{\partial \boldsymbol{C}} \otimes \dfrac{\partial \lambda_{\mathrm{fib}}^{(a)}}{\partial \boldsymbol{C}} & \text{if } \dot{D}_{(a)} > 0, \\ 0 & \text{if } \dot{D}_{(a)} = 0. \end{cases} \tag{36}$$

For the numerical implementation, discrete pseudotime steps are considered with $t \in [{}^{k+1}t, {}^k t]$ and ${}^{k+1}t$ and ${}^k t$ denoting the current and the last time step, respectively. In the current time step the trial values ${}^{k+1}y_{\mathrm{l}}^{(a)}$ and ${}^{k+1}y_{\mathrm{u}}^{(a)}$ are computed as a solution of (14). Note that due to a special choice of the random variable it may happen that only one bound occurs. If the trial value is real and inside the interval of admissible values, the following assignments are performed

$$y_{\mathrm{l}}^{(a)} = \begin{cases} {}^{k+1}y_{\mathrm{l}}^{(a)} & \text{if } {}^{k+1}y_{\mathrm{l}}^{(a)} < {}^k y_{\mathrm{l}}^{(a)}, \\ {}^k y_{\mathrm{l}}^{(a)} & \text{else,} \end{cases} \quad \text{and/or} \quad y_{\mathrm{u}}^{(a)} = \begin{cases} {}^{k+1}y_{\mathrm{u}}^{(a)} & \text{if } {}^{k+1}y_{\mathrm{u}}^{(a)} > {}^k y_{\mathrm{u}}^{(a)}, \\ {}^k y_{\mathrm{u}}^{(a)} & \text{else.} \end{cases} \tag{37}$$

Note that these case distinctions are required to ensure that no negative damage evolution ('healing') appears. In the case that a beta distributed statistical measure is considered the CDF in (15) is computed numerically according to Press et al. [48]. An overview of the algorithmic determination of the stress and elasticity tensors is summarized in Tables 1 and 2.

3. Comparative study

Here the approach presented in the previous section is used to match experimental data and to show the influence of statistical distributions of different microscopic quantities on the related mechanical response. Moreover, different strain-energy functions describing the fiber response in (6) are compared with each other. In particular, the considered transversely isotropic functions are

$$\Psi^{\mathrm{ti}}_{\mathrm{BNSH}_1,\mathrm{e}} = \frac{k_1}{2k_2}\left\{\exp\left[k_2\langle(1-D_{(a)})K_3^{(a)}-2\rangle^2\right]-1\right\}, \tag{38}$$

$$\Psi^{\mathrm{ti}}_{\mathrm{BNSH}_1,\mathrm{p}} = \alpha_1\langle(1-D_{(a)})K_3^{(a)}-2\rangle^{\alpha_2}, \tag{39}$$

$$\Psi^{\mathrm{ti}}_{\mathrm{BNSH}_2,\mathrm{p}} = \alpha_1\langle(1-D_{(a)})J_4^{(a)}-2\rangle^{\alpha_2}, \tag{40}$$

$$\Psi^{\mathrm{ti}}_{\mathrm{HGO}} = \frac{k_1}{2k_2}\left\{\exp\left[k_2\langle(1-D_{(a)})J_4^{(a)}-1\rangle^2\right]-1\right\}, \tag{41}$$

wherein the first three functions are introduced in Balzani et al. [17] and the last one in Holzapfel et al. [12]. Therefore, the resulting complete strain–energy functions are denoted accordingly by $\Psi_{\mathrm{BNSH}_1,\mathrm{e}}$, $\Psi_{\mathrm{BNSH}_1,\mathrm{p}}$, $\Psi_{\mathrm{BNSH}_2,\mathrm{p}}$, and Ψ_{HGO}, respectively. Herein, the material restrictions $k_1 > 0$, $k_2 > 0$, $\alpha_1 > 0$, and $\alpha_2 > 1$ (for smooth tangent moduli: $\alpha_2 > 2$) have to be fulfilled in order to guarantee polyconvexity of the resulting functions in the undamaged physiological domain. The parameters k_1 and α_1 have the dimension of stress, whereas k_2 and α_2 are dimensionless. The damage variable $D_{(a)}$ follows the new damage function (15).

Gaussian as well as beta distributions are considered for the individual random variables whenever it is reasonable. In detail, for the initial PG angle α (see Section 2.2.1) and for the ultimate PG stretch $\lambda_{\mathrm{pg}}^{\mathrm{sust}}$ (see Section 2.2.3) a beta distribution is considered, whereas for the internal length L (see Section 2.2.2) a Gaussian distribution is taken into account. Unfortunately, only rare information is available in the literature from which conclusions about the values of the microscopic parameters can be drawn. For the PG orientation Dell'Orbo et al. [49], Dingemans et al. [46] and Liao and Vesely [45] provide some few and specific results. Similarly, very little is known in regard to the geometry of the collagen fibrils, see, for example, Graham et al. [50] or Birk and Zycband [51], or in regard to the ultimate PG stretch. Therefore, we also adjust the microscopic parameters to the experimental data. For the adjustment the stress–stretch response of the model is compared with experimental data from the media of a human carotid artery, as documented in [34]. For this purpose the set of material parameters is assembled in a vector $\boldsymbol{\alpha}$, and the least-square function

$$\bar{r}(\boldsymbol{\alpha}) = \sum_{\mathrm{k}=1}^{n_{\mathrm{exp}}}\sqrt{\frac{1}{n_{\mathrm{mp}}}\sum_{i=1}^{n_{\mathrm{cyc}}}\sum_{j=1}^{n_{\mathrm{mp},i}} r(\boldsymbol{\alpha})} \quad \text{with } r(\boldsymbol{\alpha}) = \left(\frac{\sigma^{\mathrm{exp}}(\lambda_1^{(i,j)}) - \sigma^{\mathrm{comp}}(\lambda_1^{(i,j)},\boldsymbol{\alpha})}{\max\limits_i(\sigma^{\mathrm{exp}})}\right)^2 \tag{42}$$

is minimized with respect to $\boldsymbol{\alpha}$. The set of parameters consists of the material parameters included directly in the strain-energy function and the damage model, and in addition to this, the fiber angle β_{f}, which defines the angle between the circumferential direction of the artery and the fiber orientation. A number of $n_{\mathrm{exp}} = 2$ experiments is considered, namely cyclic uniaxial tension tests for specimens in the axial and the circumferential direction of the artery. The number of cycles i is denoted by n_{cyc} and the number of measured points j in each cycle is $n_{\mathrm{mp},i}$. The difference between the experimentally measured stress σ^{exp} and the computed stress σ^{comp} is normalized by the maximum experimental stress $\max(\sigma^{\mathrm{exp}}) \neq 0$ in the respective cycle. The number of cycles is $n_{\mathrm{cyc}} = 18$ in the axial direction and $n_{\mathrm{cyc}} = 27$ in the circumferential direction. The number of measured points is different in each individual cycle, however, a total number of $n_{\mathrm{mp}} = 1271$ for the axial and $n_{\mathrm{mp}} = 1793$ for the circumferential direction is considered. For the parameter adjustment the method as used in Balzani et al. [34] is applied. Thereby, incompressibility is assumed and an iterative procedure adjusts for the uniaxial tension conditions. Thus, the parameters of the penalty function are of course not considered for the adjustment procedure.

3.1. Distributed proteoglycan orientation

We start by considering a beta distributed PG orientation. For an improvement of the optimization procedure reasonable bounds of the individual material parameters are defined. Microscopic images showing proteoglycans are,

Table 3
Material parameters and error measure $\bar{r}$ for the models $\Psi_{\mathrm{BNSH}_1,\mathrm{e}}$, $\Psi_{\mathrm{BNSH}_1,\mathrm{p}}$, $\Psi_{\mathrm{BNSH}_2,\mathrm{p}}$ and Ψ_{HGO} for the media of a human carotid artery under consideration of a beta distributed PG orientation; see relation (6) with the use of (7), (38)–(41) and the microscopical parameters according to Section 2.2.

	c_1 (kPa) > 0	$k_1 \vert \alpha_1$ (kPa) > 0	k_2 (–) > 0	α_2 (–) > 2	β_f (°) > 22.5 < 45.0	$\lambda_{\mathrm{pg}}^{\mathrm{sust}}$ (–) > 1 < 2	L (–) > 0	a (–) > 0	b (–) > 0	$\bar{r}$ (–)
$\Psi_{\mathrm{BNSH}_1,\mathrm{e}}$	9.58	894.38	87.0	–	39.40	1.0158	3.8	9.8	18.9	0.067
$\Psi_{\mathrm{BNSH}_1,\mathrm{p}}$	9.75	1003.8	–	2.06	39.39	1.0068	4.7	5.4	13.7	0.073
$\Psi_{\mathrm{BNSH}_2,\mathrm{p}}$	20.09	4434.6	–	2.0	38.32	1.0092	6.0	8.2	16.3	0.195
Ψ_{HGO}	22.61	928.98	819.4	–	38.32	1.1295	14.5	13.7	28.9	0.221

for example, given by Dell'Orbo et al. [49], Dingemans et al. [46] and Liao and Vesely [45]. They indicate that the PG orientation is predominantly arranged in the orientation perpendicular to the fiber direction. Therefore, the mean value of the PG angle distribution is assumed to be within $\pi/4 \leq a\pi/(a+b) \leq 3\pi/4$. The parameters and their bounds for the four different energy functions (38)–(41), that are obtained by the adjustment procedure, are summarized in Table 3.

By comparing the resulting error measure $\bar{r}$ provided in Table 3 it can be seen that the function $\Psi_{\mathrm{BNSH}_1,\mathrm{e}}^{\mathrm{ti}}$ leads to the best agreement with the experimental data. Hence, the related Cauchy stress–stretch response is compared with the experimental data in Fig. 4(a), while the distribution of the error measure r is illustrated in Fig. 4(b). A good correlation with the experimental data is observed.

For completeness the results for the other three strain–energy functions (39)–(41) are provided in Fig. 11 in the Appendix B.1. Using the functions $\Psi_{\mathrm{BNSH}_2,\mathrm{p}}$ and Ψ_{HGO} no adequate reproduction of the softening hysteresis is achieved. One reason might be that in the latter models solely the fourth mixed invariant of the right Cauchy–Green tensor and the structural tensor is considered and, therefore, the fiber response is captured in a rather stiff form. In some sense the functions $\Psi_{\mathrm{BNSH}_1,\mathrm{e}}$ and $\Psi_{\mathrm{BNSH}_1,\mathrm{p}}$ include this feature since the effective transversely isotropic function $\Psi_{(a)}^{\mathrm{ti},0} = K_3^{(a)} = \|\mathrm{Cof}[\boldsymbol{F}]\|^2 - \|\mathrm{Cof}[\boldsymbol{F}]\boldsymbol{A}_{(a)}\|^2$ describes the deformation of an area element oriented in the direction perpendicular to the fiber direction.

3.2. Distributed internal length

Here we study the internal length L, which is assumed to be Gaussian distributed. The definition of meaningful bounds for the mean value of the internal length L, as defined in (13), is rather tricky because the collagen fibril length L_{cf}, the initial overlap L_{ov} of two fibrils and the initial transverse distance d_0 between collagen fibrils are difficult to measure. It appears that there is very little in the literature regarding appropriate measurements of these parameters. Specific values are, for example, provided for the collagen fibril length, which, however, ranges from 1 to 170 μm depending on the tissue type, see [50,51]. In addition, the available data is not related to human arterial tissue. Thus, here the mean value is just assumed to be positive.

In the following we adjust the models $\Psi_{\mathrm{BNSH}_1,\mathrm{e}}$ and $\Psi_{\mathrm{BNSH}_1,\mathrm{p}}$ to experimental data. The optimization yields comparable results in terms of the error measure $\bar{r}$, see Table 4.

Fig. 4(c), (d) provide the resulting Cauchy stress–stretch response for the model $\Psi_{\mathrm{BNSH}_1,\mathrm{e}}$, where a negligible softening hysteresis is observed, and the error measure r. One reason is that the induced damage is rather small at these deformations. The response of model $\Psi_{\mathrm{BNSH}_1,\mathrm{p}}$ does not yield a better correlation with the experiment although some softening hysteresis is observed, see Fig. 12(a), (b) in Appendix B.2. Apparently, a statistical distribution of the PG orientation has a larger capability of yielding a softening hysteresis observed in experiments.

3.3. Distributed ultimate proteoglycan stretch

Finally, beta distributions of the ultimate PG stretch $\lambda_{\mathrm{pg}}^{\mathrm{sust}}$ are taken into account. Again, comparable results in terms of the error measure $\bar{r}$ are obtained for the functions $\Psi_{\mathrm{BNSH}_1,\mathrm{e}}$ and $\Psi_{\mathrm{BNSH}_1,\mathrm{p}}$, see Table 5.

Here, the response of the model $\Psi_{\mathrm{BNSH}_1,\mathrm{p}}$ yields a slightly smaller error $\bar{r}$. The Cauchy stress–stretch response of both models provides a qualitatively good reproduction of the experiment, see Fig. 4(e), (f) and Fig. 12(c), (d) in

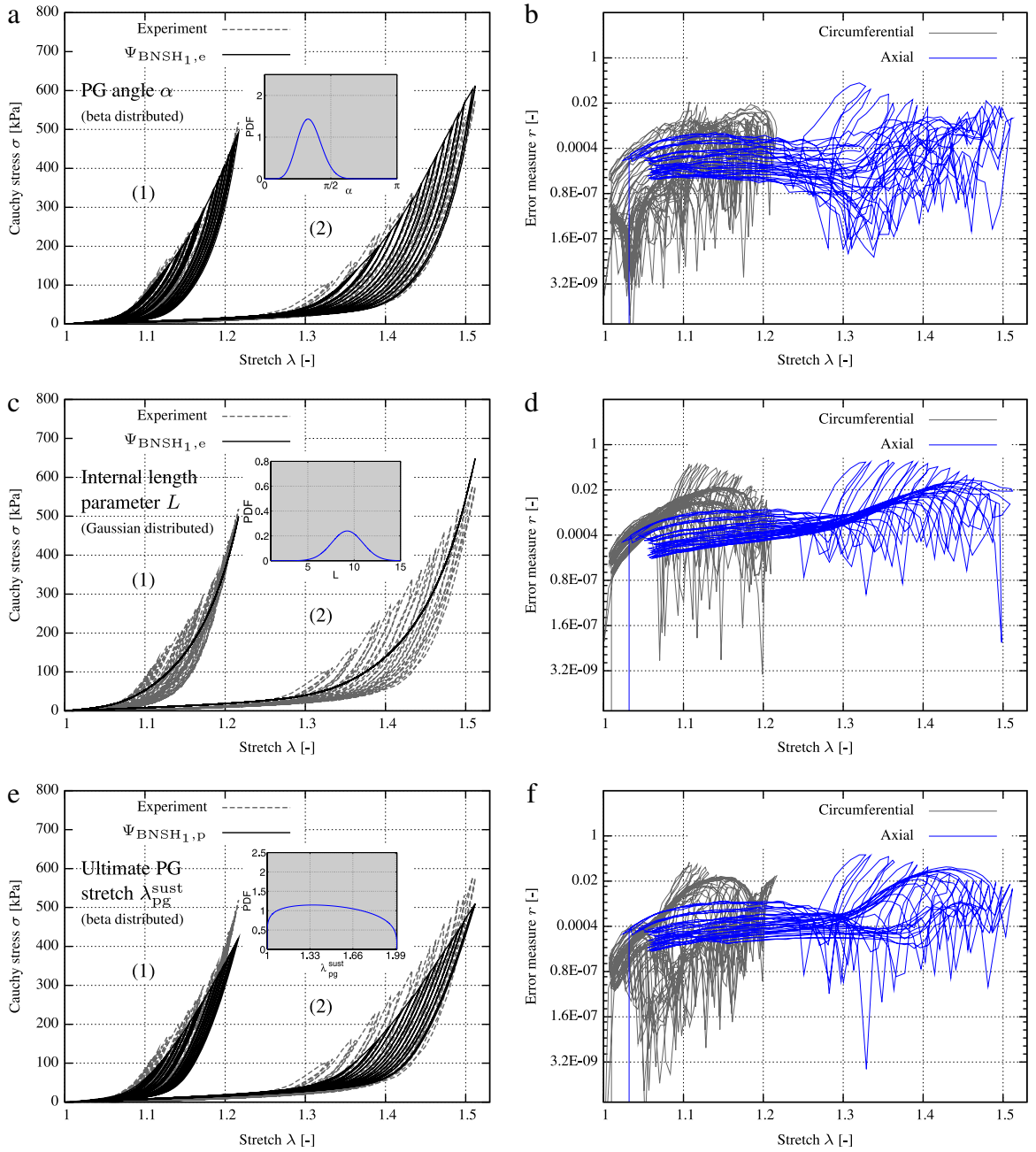

Fig. 4. Cyclic uniaxial tension tests of the media of a human carotid artery in circumferential (1) and axial (2) directions, as also documented in [34]: (a) experimental data and results of the constitutive model $\Psi_{\mathrm{BNSH}_1,\mathrm{e}}$, PG angle α is beta distributed, material parameters are taken from Table 3; (c) experimental data and model $\Psi_{\mathrm{BNSH}_1,\mathrm{e}}$, internal length L is Gaussian distributed, material parameters are taken from Table 4. Note that the cyclic protocol is also applied to the model. But since the induced damage values are too small no visible hysteresis is obtained; (e) experimental data and model $\Psi_{\mathrm{BNSH}_1,\mathrm{p}}$, ultimate PG stretch $\lambda_{\mathrm{pg}}^{\mathrm{sust}}$ is beta distributed, material parameters are taken from Table 5; (b), (d), (f) related error measure r.

Appendix B.2. Quantitatively, however, the results are not as good as for the case of a statistically distributed PG orientation. Therefore, a statistical distribution of the PG orientation may have the most significant influence on the damage behavior compared with the other investigated quantities. Even though the stress response of some of the models captures the experimentally observed softening quite well, the obtained values of the microscopic parameters for the damage model require further experimental investigation on the microscale.

Table 4
Material parameters and error measure $\bar{r}$ for the models $\Psi_{\mathrm{BNSH}_1,\mathrm{e}}$ and $\Psi_{\mathrm{BNSH}_1,\mathrm{p}}$ for the media of a human carotid artery under consideration of a Gaussian distributed internal length L; see relation (6) with the use of (7), (38), (39) and the microscopical parameters according to Section 2.2.

	c_1 (kPa) >0	$k_1\|\alpha_1$ (kPa) >0	k_2 (–) >0	α_2 (–) >2	β_f (°) >22.5 <45.0	$\lambda_\mathrm{pg}^\mathrm{sust}$ (–) >1 <2	α (–) $>\frac{\pi}{4}$ $<\frac{3\pi}{4}$	μ (–) >0	σ_D (–) >0	$\bar{r}$ (–)
$\Psi_{\mathrm{BNSH}_1,\mathrm{e}}$	11.796	541.94	30.2	–	39.10	1.0161	0.91	9.3	1.67	0.1766
$\Psi_{\mathrm{BNSH}_1,\mathrm{p}}$	7.671	717.83	–	2.3	39.42	1.1301	1.97	2.9	0.62	0.1768

Table 5
Material parameters and error measure $\bar{r}$ for the models $\Psi_{\mathrm{BNSH}_1,\mathrm{e}}$ and $\Psi_{\mathrm{BNSH}_1,\mathrm{p}}$ for the media of a human carotid artery under consideration of a beta distributed ultimate PG stretch $\lambda_\mathrm{pg}^\mathrm{sust}$; see relation (6) with the use of (7), (38), (39) and the microscopical parameters according to Section 2.2.

	c_1 (kPa) >0	$k_1\|\alpha_1$ (kPa) >0	k_2 (–) >0	α_2 (–) >2	β_f (°) >22.5 <45.0	α (–) $>\frac{\pi}{4}$ $<\frac{3\pi}{4}$	L (–) >0	a (–) >0	b (–) >0	$\bar{r}$ (–)
$\Psi_{\mathrm{BNSH}_1,\mathrm{e}}$	13.137	541.3	115.8	–	39.17	2.3562	3.6	1.70	0.96	0.135
$\Psi_{\mathrm{BNSH}_1,\mathrm{p}}$	12.014	2578.4	–	2.6	39.24	2.3549	1.4	1.16	1.29	0.141

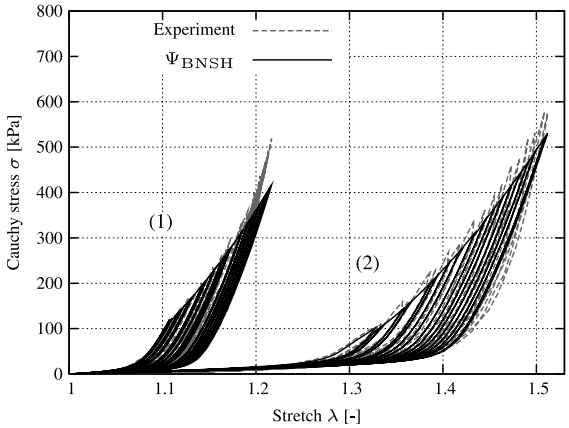

Fig. 5. Cyclic uniaxial tension tests for the media of a human carotid artery in circumferential (1) and axial (2) directions, as also documented in [34]: experimental data and results of the constitutive model Ψ_{BNSH} from [34] (cf. Fig. 4(b) therein). The error measure is $\bar{r} = 0.08$.

3.4. Comparison with phenomenological damage function

In order to analyze the benefits of the proposed approach compared to the phenomenological model in Balzani et al. [34], we compare the stress–stretch response resulting from a distributed PG orientation, since this leads to the best adjustment to experimental data in terms of the error measure $\bar{r}$. Fig. 5 shows the Cauchy stress versus the stretch of the phenomenological model given in [34] for a uniaxial tension test. As can be seen, the qualitative accordance to the experiment is comparable to the results obtained by the new approach presented here. Quantitatively, however, the error for the new model $\bar{r} = 0.067$ is approximately 16% lower than the error for the phenomenological model ($\bar{r} = 0.08$).

4. Representative numerical examples

The performance of the described damage model is demonstrated by representative numerical examples. The model is implemented in the finite element analysis program FEAP (Prof. R. Taylor, University of California Berkeley). In

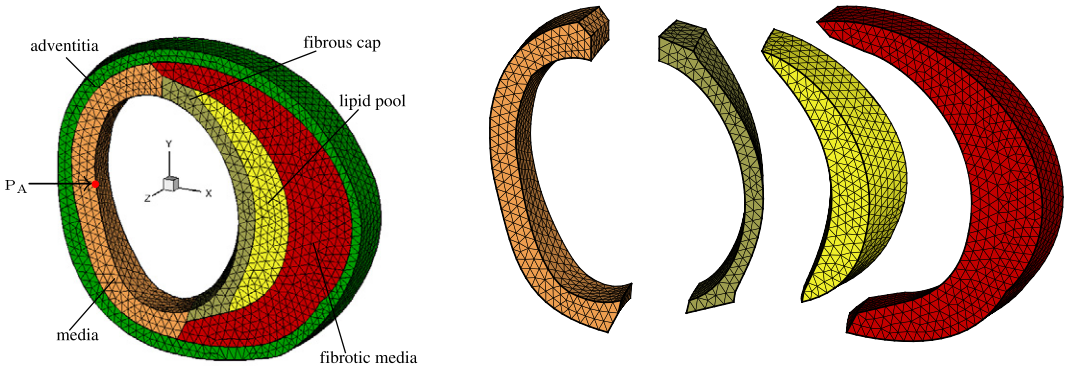

Fig. 6. Finite element model 1: a thin three-dimensional section of a diseased artery with five different tissue layers discretized with 21 835 quadratic tetrahedral elements. The latter discretization is the finest one used within a convergence study (see Fig. 7(b)), which is carried out for the depicted section. Thereby, beside other measures also the absolute nodal displacement of point P_A is investigated, which is marked in the left picture by a red circle.

Table 6
Hyperelastic and damage parameters of four tissue components. Parameters for the non-diseased media are taken from Table 3.

	c_1 (kPa)	$k_1 \vert \alpha_1$ (kPa)	$k_2 \vert \alpha_2$ (–)	β_f (°)	λ_{pg}^{sust} (–)	L (–)	a (–)	b (–)	$\bar{r}$ (–)
Adventitia	5.7	8159.4	3.5	45.59	1.1235	9.746	8.11	24.33	0.1213
Fibrotic media	20.9	479.36	293.3	25.18	1.0068	4.711	5.42	13.67	0.0177
Fibrous cap	27.3	1222.4	2.0	50.93	1.0068	4.711	5.42	13.67	0.0367
Lipid pool	5.0	–	–	–	–	–	–	–	–

particular we numerically compute a circumferential overstretch of atherosclerotic arteries with the goal to analyze the applicability and robustness of the proposed approach within a finite element program.

In a first step an FE convergence study is performed in order to determine a reasonable discretization. Therefore, a thin simplified section of a diseased artery with 0.5 cm thickness and the following multiple tissue layers is considered (cf. [52]): fibrous cap, lipid pool, (diseased) fibrotic media, (non-diseased) media, adventitia, see Fig. 6. As it can be seen in Fig. 6 (right hand side) the structural geometry of the individual layers also changes in the axial direction to capture some slight three-dimensional distributions of the mechanical fields.

The model is discretized with quadratic tetrahedral elements. For the convergence study, six different discretizations are considered resulting in 355, 2457, 4908, 8747, 11 039, and 21 835 elements. Fig. 6 shows the finest discretization. Therein, also the point P_A, for which the absolute nodal displacement is analyzed, is marked by a red circle. Since some parts of the strain-energy function contain cofactor terms of the right Cauchy–Green tensor, improved finite element convergence might be obtained when using the five-field element formulation, as proposed by Schröder et al. [53]. For the non-diseased media the strain-energy function $\Psi_{\mathrm{BNSH}_1,\mathrm{p}}$ with the parameters given in Table 3 is used. For the other layers, except for the lipid pool, the individual functions were also adjusted to experimental data, and the functions that yielded the best response were chosen. In more detail $\Psi_{\mathrm{BNSH}_1,\mathrm{e}}$ is used for the fibrotic media and $\Psi_{\mathrm{BNSH}_1,\mathrm{p}}$ is applied to the fibrous cap and the adventitia. For the adventitia the model was adjusted to the experimental data given in [34]. Since no cyclic tension tests in the supra-physiological loading domain are available for the fibrous cap and the fibrotic media, hyperelastic parameters were adjusted to the experimental data of human atherosclerotic plaques, as documented in [54]. For the damage parameters the same values as obtained by adjusting to the media were taken for these components. The lipid pool is considered as a butter-like, incompressible material [54], and is, therefore, modeled by a neo-Hookean material. Due to the lack of experimental data the parameter for the lipid pool is chosen such that the stiffness is significantly lower than in the remaining components; damage is not considered in the lipid pool. A summary of all parameters with the resulting error measure $\bar{r}$ is given in Table 6.

To control the volumetric behavior the penalty function $\Psi^{\mathrm{pen}} = \epsilon_1 \left(I_3^{\epsilon_2} + I_3^{-\epsilon_2} - 2 \right)$ is used. The parameters ϵ_1 and ϵ_2 are chosen such that the quasi-incompressibility constraint $\det \boldsymbol{F} = 1 \pm 1\%$ is fulfilled at any location in the artery. In more detail we have set $\epsilon_1 = 50.0$ kPa and $\epsilon_2 = 20.0$ for the adventitia, the non-diseased media, the fibrotic

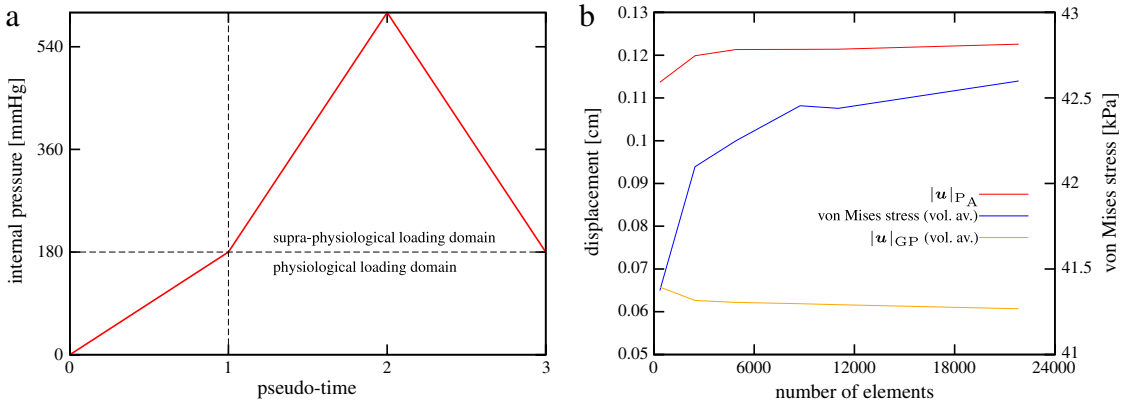

Fig. 7. (a) Applied loading protocol for both numerical examples described in this section; (b) results of the convergence study for model 1: depicted are the absolute nodal displacement $|\boldsymbol{u}|_{\mathrm{P_A}}$ of the point $\mathrm{P_A}$, which is marked by a red circle in Fig. 6, as well as the volume averages of the absolute displacements $|\boldsymbol{u}|_{\mathrm{GP}}$ at the Gauss points and of the von Mises stress at pseudotime = 3 of the applied loading protocol. For the convergence study discretizations with 355, 2457, 4908, 8747, 11 039, and 21 835 elements are investigated.

media and the fibrous cap, and $\epsilon_1 = 20.0$ kPa and $\epsilon_2 = 10.0$ for the lipid pool. The applied internal pressure, which follows the loading protocol depicted in Fig. 7(a), is first increased up to 24.0 kPa ($\hat{=}$180.0 mmHg) which may be interpreted as the very upper limit of the physiological blood pressure. In order to incorporate residual axial stretches an axial strain of 4% is applied simultaneously to the inflation of the artery. Residual strains in the circumferential direction are neglected, because their related circumferential stresses are significantly lower compared to the stresses that occur during a circumferential overstretch. Since damage mainly evolves in highly overstretched regions, we deduce that this omission is acceptable for a damage calculation. The internal pressure is then increased to a maximum of 80.0 kPa ($\hat{=}$600.0 mmHg) yielding the overstretched state of the artery. Then the pressure is decreased again to the physiological blood pressure. This situation enables the analysis of the influence of damage due to overstretch on the physiological state. For the convergence study, the marked nodal point $\mathrm{P_A}$ in Fig. 6 is regarded. For the latter point, the absolute nodal displacement $|\boldsymbol{u}|_{\mathrm{P_A}}$ is compared for each considered discretization at pseudotime = 3 (cf. Fig. 7(a)). Furthermore, for every discretization the volume averages over the complete artery of the absolute displacements at the Gauss points $|\boldsymbol{u}|_{\mathrm{GP}}$ as well as the von Mises stress are computed at pseudotime = 3. The results of the convergence study are depicted in Fig. 7(b). The model shows a converging response with increasing number of elements. We deduce, that approximately 6000 elements are sufficient to obtain results for an arterial segment with the width of 0.5 cm. For the study of damage and remanent strains an additional idealized section of a diseased artery is analyzed which is ten times longer, and which should therefore be discretized with at least 60 000 elements. Here, the artery, as depicted in Fig. 8, is considered and discretized with 61 858 tetrahedral elements. The material properties as well as the applied loading protocol and the applied percentage of pre-stretch are chosen identically to the first model (see Fig. 6).

Fig. 9 depicts the resulting damage distribution for both investigated models at an internal pressure of $p = 80.0$ kPa (pseudotime = 2). Thereby, the computation with the highest number of elements is considered for model 1. In both models, high damage values are observed in the healthy media as well as in the fibrous cap, see Fig. 9. These observations are in line with the findings from Balzani et al. [34]. Interestingly, for the longer artery a severe damage concentration is also observed in the healthy media next to the plaque in the axial direction (area with high damage values at the bottom right of Fig. 9(b)). A rather low damage is found in the adventitia. The microscopic damage yields not only a softening of the material but also remanent strains in the fibers such that larger fiber stretches should be expected under physiological loading after overstretch. This is shown in Fig. 10 for model 2, where an increased fiber stretch $\lambda_{\mathrm{fib}}^{(1)}$ is observed in the physiological situation after the overstretch.

5. Conclusion

In this paper a statistical approach was proposed to describe microscopic damage evolution in soft collagenous tissues. Three statistically distributed microscopic quantities were analyzed for their capability to yield the distinct

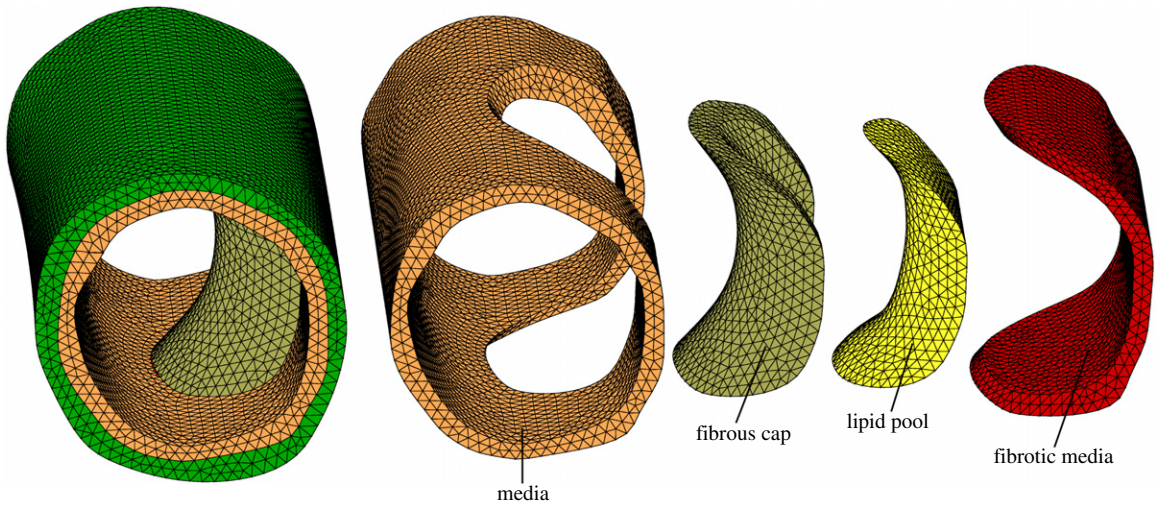

Fig. 8. Finite element model 2: longer three-dimensional section of a diseased artery discretized with 61 858 quadratic tetrahedral elements.

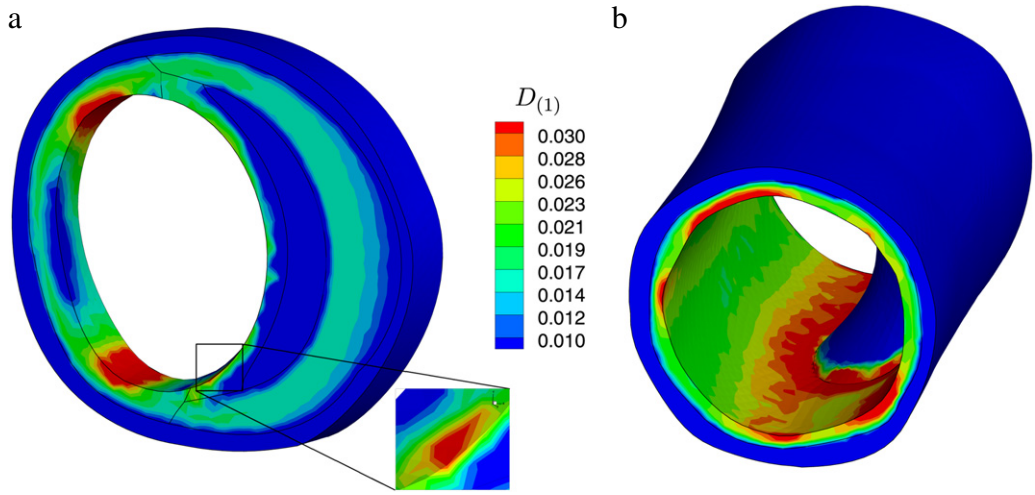

Fig. 9. Distribution of the damage variable $D_{(1)}$ at an internal pressure of 80 kPa in (a) model 1 with 21 835 elements and in (b) model 2.

softening hysteresis that can be observed when subjecting soft collagenous tissues such as arterial walls to cyclic loading in the supra-physiological domain. To consider the different statistical distributions a new statistically-based damage function was introduced and embedded in a constitutive framework for modeling damage from Balzani et al. [34]. Different constitutive models have been adjusted to experimental data of a human carotid artery and it turned out that depending on the choice of the random variable and strain-energy function a good correlation with experiments can be obtained. It was found that under the considered assumptions a statistical distribution of the initial proteoglycan orientation within the collagen fibrils has the most significant influence on the tissue's softening behavior. For the latter case, the accuracy with respect to the model's ability to represent experimental data was found to be improved compared to the phenomenological model from [34]. However, it is emphasized again, that the main advantage of the proposed damage model over purely phenomenological approaches has to be seen in the physical interpretability of its parameters. Two simplified three-dimensional atherosclerotic arteries were simulated in order to show that the implementation of the new damage model works within a finite element framework. Both models were circumferentially overstretched, which resulted in large damage values in the healthy media and in the fibrous cap, respectively. Furthermore, we observed increased deformations under physiological loading after the circumferential overstretch.

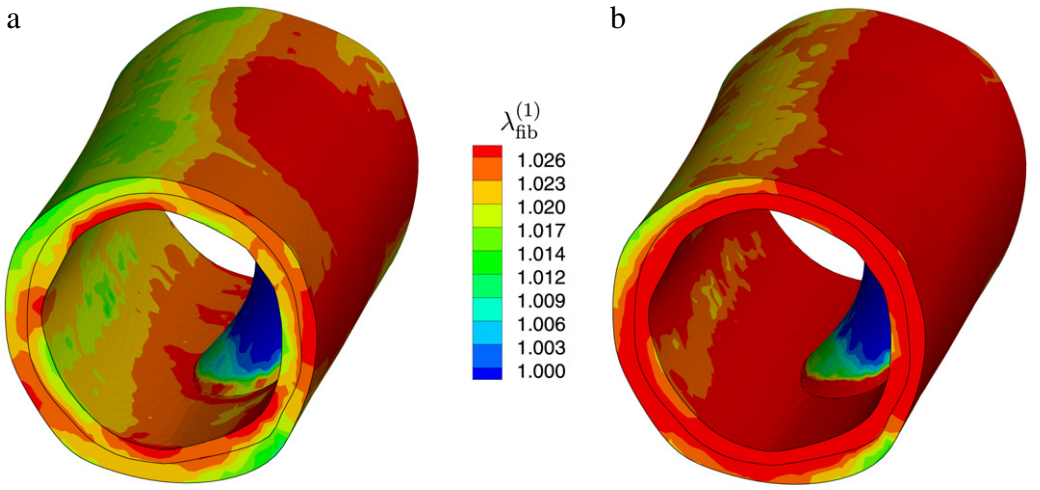

Fig. 10. Distribution of the fiber stretch $\lambda_{fib}^{(1)}$ in model 2 under physiological blood pressure (24 kPa) (a) before and (b) after circumferential overstretch.

Acknowledgments

The authors greatly appreciate the financial support of the Deutsche Forschungsgemeinschaft (DFG), research grant BA 2823/5-1, and the FWF Austrian Science Fund, research grant I 503-B11. Further thanks go to Gerhard Sommer, who carried out the experiments.

Appendix A. Abbreviations

The following abbreviations have been used for Eqs. (19) and (20):

$$a_1 = {\lambda_{fib}}^2$$
$$a_2 = \lambda_{pg}^{sust2}$$
$$a_3 = {\lambda_{fib}}^4 L^2$$
$$a_4 = L^2 a_1$$
$$a_5 = 2L^2 {\lambda_{fib}}^3$$
$$a_6 = L^2 {\lambda_{fib}}^4 a_2$$
$$a_7 = \sqrt{(\lambda_{fib}-1)^2 {\lambda_{fib}}^3 L^2 \left(L^2 {\lambda_{fib}}^3 a_2 - 2a_4 a_2 + a_2 \lambda_{fib} - \lambda_{pg}^{sust4} \lambda_{fib} + L^2 \lambda_{fib} a_2 + a_2 - 1\right)}$$
$$a_8 = (\lambda_{fib}-1)^2$$
$$a_9 = L^4 {\lambda_{fib}}^4$$
$$a_{10} = L^4$$
$$a_{11} = {\lambda_{fib}}^3$$
$$a_{12} = 2L^2 \lambda_{fib}$$
$$a_{13} = a_{10} {\lambda_{fib}}^5$$
$$a_{14} = \sqrt{L^2 a_{11} a_8 \left(L^2 a_{11} a_2 - 2a_4 a_2 - \lambda_{pg}^{sust4} \lambda_{fib} + L^2 \lambda_{fib} a_2 + a_2 \lambda_{fib} - 1 + a_2\right)}$$
$$a_{15} = a_1 - a_2 a_1 + a_2 \lambda_{fib} + a_3 + a_4 - a_5 + a_4 a_2 - a_5 a_2 - \lambda_{fib} + a_6 + 2a_7$$
$$a_{16} = \sqrt{\frac{a_{15}}{a_8 (a_9 - 2a_{10} a_{11} + 2a_4 + a_{10} a_1 + a_{12} + 1)}}$$

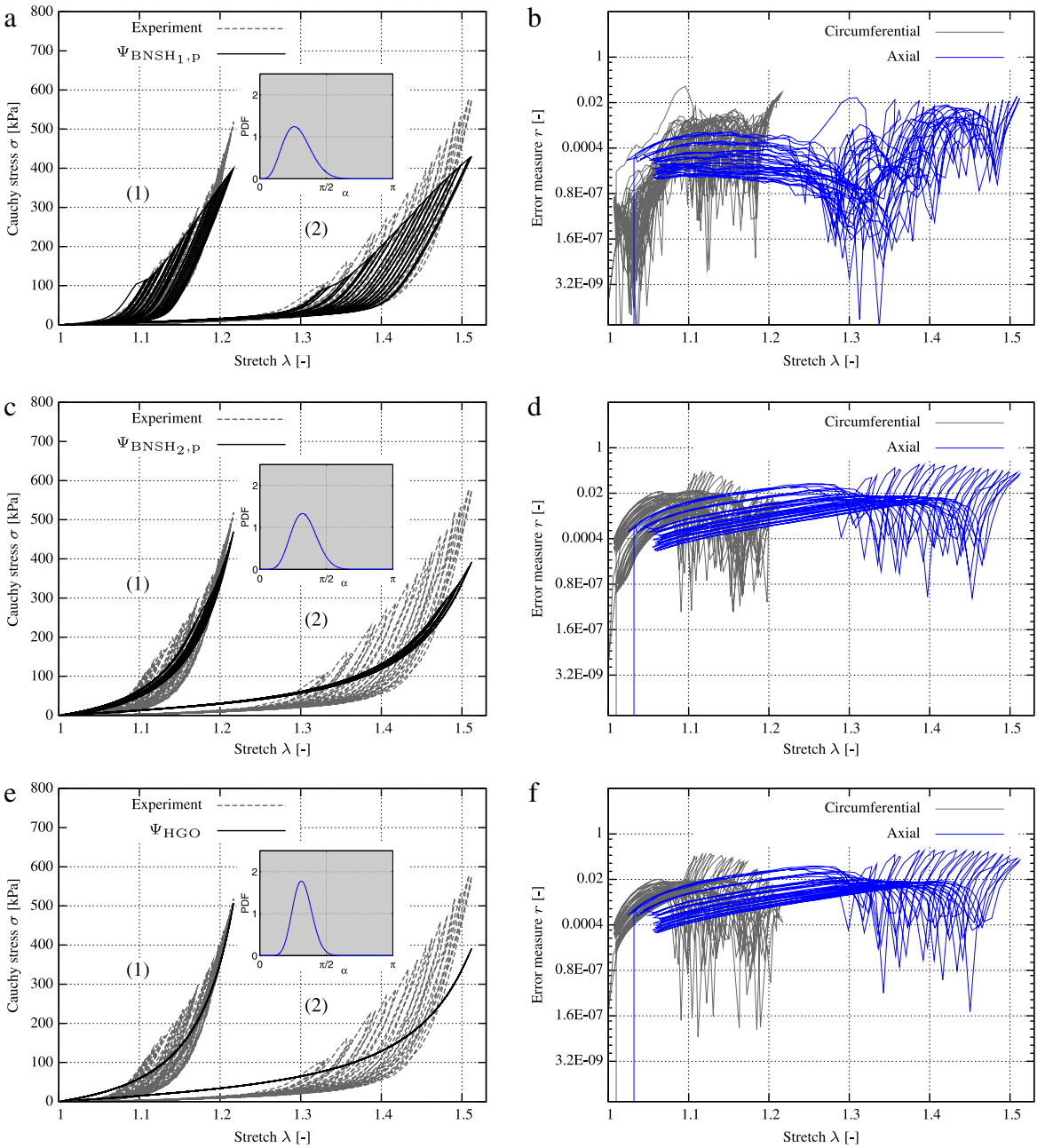

Fig. 11. Cyclic uniaxial tension tests of the media of a human carotid artery in circumferential (1) and axial (2) directions, as also documented in [34]: experimental data and results of the constitutive model (a) $\Psi_{\mathrm{BNSH}_1,\mathrm{p}}$, (c) of $\Psi_{\mathrm{BNSH}_2,\mathrm{p}}$, and (e) of Ψ_{HGO}; (b), (d), (f) related error measure r. The material parameters are taken from Table 3. The PG angle α is beta distributed.

$$a_{17} = \sqrt{\frac{-\lambda_{\mathrm{fib}} + a_3 - a_5 a_2 + a_1 + a_4 a_2 + a_2 \lambda_{\mathrm{fib}} + a_6 - a_5 + a_4 - a_2 a_1 - 2a_{14}}{a_8 \left(a_9 - 2a_{10} a_{11} + a_{10} a_1 + 2a_4 + a_{12} + 1\right)}}$$

$$a_{18} = a_{10} {\lambda_{\mathrm{fib}}}^6 - 3a_{13}$$

$$a_{19} = \left(a_{13} - 3a_9 + a_5 + 3a_{10} a_{11} - a_{10} a_1 - a_{12} + \lambda_{\mathrm{fib}} - 1\right)\left(\lambda_{\mathrm{fib}} - 1\right) \lambda_{\mathrm{fib}} L$$

$$a_{20} = a_{18} + 3a_9 + a_3 - 2a_6 + a_5 a_2 - a_{10} a_{11} - a_4.$$

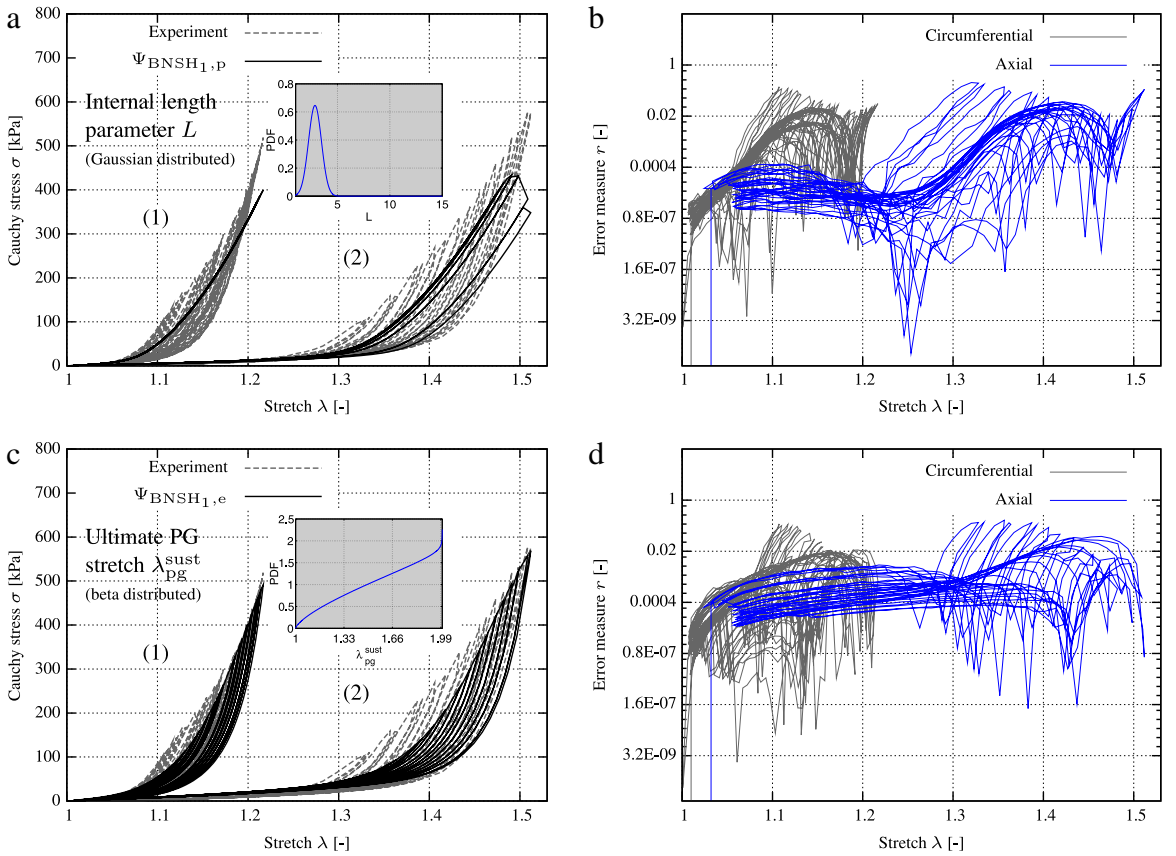

Fig. 12. Cyclic uniaxial tension tests of the media of a human carotid artery in circumferential (1) and axial (2) directions: (a) experimental data and results of model $\Psi_{\mathrm{BNSH}_1,\mathrm{p}}$, internal length L is Gaussian distributed, material parameters are taken from Table 4; (c) experimental data and model $\Psi_{\mathrm{BNSH}_1,\mathrm{e}}$, ultimate PG stretch $\lambda_{\mathrm{pg}}^{\mathrm{sust}}$ is beta distributed, material parameters are taken from Table 5; (b), (d) related error measure r.

Appendix B. Stress–strain response of three model functions

B.1. Distributed proteoglycan orientation

See Fig. 11.

B.2. Distributed internal length and ultimate proteoglycan stretch

See Fig. 12.

References

[1] Y.C. Fung, Biomechanics–Mechanical Properties of Living Tissues, second ed., Springer, New York, Berlin, Heidelberg, 1993.
[2] H. Abé, K. Hayashi, M. Sato (Eds.), Data Book on Mechanical Properties of Living Cells, Tissues, and Organs, Springer Verlag, New York, 1996.
[3] J.D. Humphrey, Cardiovascular Solid Mechanics. Cells, Tissues, and Organs, Springer-Verlag, New York, 2002.
[4] G.A. Holzapfel, R.W. Ogden (Eds.), Mechanics of Biological Tissue, Springer-Verlag, Heidelberg, 2006.
[5] W.R. Castaneda-Zuniga, A. Formanek, M. Tadavarthy, Z. Vlodaver, J.E. Edwards, C. Zollikofer, K. Amplatz, The mechanism of balloon angioplasty, Radiology 135 (1980) 565–571.
[6] H.S. Oktay, T. Kang, J.D. Humphrey, G.G. Bishop, Changes in the mechanical behavior of arteries following balloon angioplasty, in: R.L. Spilker, M.H. Friedman (Eds.), in: ASME 1991 Biomechanics Symposium, AMD-Vol.120, The American Society of Mechanical Engineers, 1991.

[7] G.A. Holzapfel, C.A.J. Schulze-Bauer, M. Stadler, Mechanics of angioplasty: wall, balloon and stent, in: J. Casey, G. Bao (Eds.), in: Mechanics in Biology, AMD-Vol. 242/BED-Vol. 46, The American Society of Mechanical Engineers (ASME), New York, 2000, pp. 141–156.
[8] C.A.J. Schulze-Bauer, P. Regitnig, G.A. Holzapfel, Mechanics of the human femoral adventitia including the high-pressure response, Amer. J. Physiol. Heart Circ. Physiol. 282 (2002) H2427–H2440.
[9] G. Sommer, P. Regitnig, L. Költringer, G.A. Holzapfel, Biaxial mechanical properties of intact and layer-dissected human carotid arteries at physiological and supra-physiological loadings, Am. J. Physiol. Heart Circ. Physiol. 298 (2010) H898–912.
[10] H. Weisbecker, D.M. Pierce, P. Regitnig, G.A. Holzapfel, Layer-specific damage experiments and modeling of human thoracic and abdominal aortas with non-atherosclerotic intimal thickening, J. Mech. Behav. Biomed. Mater. 12 (2012) 93–106.
[11] J.M. Ball, Constitutive inequalities and existence theorems in nonlinear elastostatics, in: R.J. Knops (Ed.), Symposium on Non-Well Posed Problems and Logarithmic Convexity, in: Springer-Lecture Notes in Math., vol. 316, 1977.
[12] G.A. Holzapfel, T. Gasser, R. Ogden, A new constitutive framework for arterial wall mechanics and a comparative study of material models, J. Elasticity 61 (2000) 1–48.
[13] M. Itskov, A. Aksel, A class of orthotropic and transversely isotropic hyperelastic constitutive models based on a polyconvex strain energy function, Int. J. Solids Struct. 41 (2004) 3833–3848.
[14] D. Balzani, Polyconvex anisotropic energies and modeling of damage applied to arterial walls (Ph.D. thesis) University Duisburg–Essen, Verlag Glückauf Essen, 2006.
[15] A. Ehret, M. Itskov, A polyconvex hyperelastic model for fiber-reinforced materials in application to soft tisues, J. Mech. Phys. Solids 42 (2007) 8853–9963.
[16] J. Schröder, P. Neff, Invariant formulation of hyperelastic transverse isotropy based on polyconvex free energy functions, Int. J. Solids Struct. 40 (2003) 401–445.
[17] D. Balzani, P. Neff, J. Schröder, G.A. Holzapfel, A polyconvex framework for soft biological tissues. Adjustment to experimental data, Int. J. Solids Struct. 43 (20) (2006) 6052–6070.
[18] J.C. Simo, On a fully three-dimensional finite-strain viscoelastic damage model: formulation and computational aspects, Comput. Methods Appl. Mech. Engrg. 60 (1987) 153–173.
[19] S. Govindjee, J.C. Simo, A micro-mechanically based continuum damage model for carbon black-filled rubbers incorporating Mullins' effect, J. Mech. Phys. Solids 39 (1991) 87–112.
[20] C. Miehe, Discontinuous and continuous damage evolution in Ogden-type large-strain elastic materials, Eur. J. Mech. A Solids 14 (1995) 697–720.
[21] C. Miehe, J. Keck, Superimposed finite elastic–viscoelastic–plastoelastic stress response with damage in filled rubbery polymers. Experiments, modelling and algorithmic implementation, J. Mech. Phys. Solids 48 (2000) 323–365.
[22] R. Dargazany, M. Itskov, A network evolution model for the anisotropic Mullins effect in carbon black filled rubbers, Int. J. Solids Struct. 46 (16) (2009) 2967–2977.
[23] R.W. Ogden, D.G. Roxburgh, An energy-based model of the Mullins effect, in: A. Dorfmann, A. Muhr (Eds.), Proc. First European Conference on Constitutive Models, A.A. Balkema, Rotterdam, Brookfield, 1999, pp. 23–28.
[24] R.W. Ogden, D.G. Roxburgh, A pseudo-elastic model for the Mullins effect in filled rubber, Proc. R. Soc. Lond. A 455 (1999) 2861–2877.
[25] A. Dorfmann, R.W. Ogden, A constitutive model for the Mullins effect with permanent set in particle-reinforced rubber, Int. J. Solids Struct. 41 (7) (2004) 1855–1878.
[26] L.A. Gracia, E. Peña, J.M. Royo, J.L. Pelegay, B. Calvo, A comparison between pseudo-elastic and damage models for modelling the Mullins effect in industrial rubber components, Mech. Res. Commun. 36 (2009) 769–776.
[27] G.A. Francfort, J.J. Marigo, Stable damage evolution in a brittle continuous medium, Eur. J. Mech. A Solids 12 (1993) 149–189.
[28] G.A. Francfort, A. Garroni, A variational view of partial brittle damage evolution, Arch. Ration. Mech. Anal. 182 (2006) 125–152.
[29] E. Gürses, C. Miehe, On evolving deformation microstructures in non-convex partially damaged solids, J. Mech. Phys. Solids 59 (2011) 1268–1290.
[30] D. Balzani, M. Ortiz, Relaxed incremental variational formulation for damage at large strains with application to fiber-reinforced materials and materials with truss-like microstructures, Int. J. Numer. Methods Eng. 92 (2012) 551–570.
[31] D. Balzani, J. Schröder, D. Gross, Simulation of discontinuous damage incorporating residual stresses in circumferentially overstretched atherosclerotic arteries, Acta Biomater. 2 (6) (2006) 609–618.
[32] T.C. Gasser, G.A. Holzapfel, Finite element modeling of balloon angioplasty by considering overstretch of remnant non-diseased tissues in lesions, Comput. Mech. 40 (2007) 47–60.
[33] A.E. Ehret, M. Itskov, Modeling of anisotropic softening phenomena: application to soft biological tissues, Int. J. Plast. 25 (2009) 901–919.
[34] D. Balzani, S. Brinkhues, G.A. Holzapfel, Constitutive framework for the modeling of damage in collagenous soft tissues with application to arterial walls, Comput. Methods Appl. Mech. Engrg. 213–216 (2012) 139–151.
[35] B. Calvo, E. Peña, M.A. Martínez, M.A. Doblaré, An uncoupled directional damage model for fibered biological soft tissues, Int. J. Numer. Methods Eng. 69 (2007) 2036–2057.
[36] A.N. Natali, P.G. Pavan, E.L. Carniel, C. Dorow, A transversally isotropic elasto-damage constitutive model for the periodontal ligament, Comput. Methods Biomech. Biomed. Eng. 6 (2003) 329–336.
[37] P. Saez, V. Alastrué, E. Peña, M. Doblaré, Anisotropic microsphere-based approach to damage in soft fibered tissue, Biomech. Model. Mechanobiol. 11 (2012) 595–608.
[38] E. Peña, Damage functions of the internal variables for soft biological fibred tissues, Mech. Res. Commun. 38 (2011) 610–615.
[39] J.F. Rodríguez, F. Cacho, J.A. Bea, M. Doblaré, A stochastic-structurally based three dimensional finite-strain damage model for fibrous soft tissue, J. Mech. Phys. Solids 54 (2006) 864–886.
[40] J.E. Scott, Elasticity in extracellular matrix 'shape modules' of tendon, cartilage, etc. a sliding proteoglycan-filament model, J. Physiol. 553 (2) (2003) 335–343.

[41] A.J.M. Spencer, Part III. Theory of invariants, in: A.C. Eringen (Ed.), Continuum Physics, in: Mathematics, vol. I, Academic Press, New York, 1971, pp. 239–353.
[42] J.P. Boehler, Introduction to the invariant formulation of anisotropic constitutive equations, in: J.P. Boehler (Ed.), Applications of Tensor Functions in Solid Mechanics, Springer, 1987, pp. 13–30. Number 292 in Courses and Lectures of CISM.
[43] Q.-S. Zheng, A.J.M. Spencer, Tensors which characterize anisotropies, Int. J. Eng. Sci. 31 (5) (1993) 679–693.
[44] T.C. Gasser, An irreversible constitutive model for fibrous soft biological tissue: a 3-d microfiber approach with demonstrative application to abdominal aortic aneurysms, Acta Biomater. 7 (6) (2011) 2457–2466.
[45] J. Liao, I. Vesely, Skewness angle of interfibrillar proteoglycans increases with applied load on mitral valve chordae tendineae, J. Biomech. 40 (2007) 390–398.
[46] K.P. Dingemans, P. Teeling, J.H. Lagendijk, A.E. Becker, Extracellular matrix of the human aortic media: an ultrastructural histochemical and immunohistochemical study of the adult aortic media, Anat. Rec. 258 (1) (2000) 1–14.
[47] G.A. Holzapfel, Nonlinear Solid Mechanics. A Continuum Approach for Engineering, John Wiley & Sons, Chichester, 2000.
[48] W.H. Press, B.P. Flannery, S.A. Teukolsky, W.T. Vetterling, Numerical Recipes in Fortran 77: The Art of Scientific Computing, second ed., Cambridge University Press, 1992.
[49] C. Dell'Orbo, G. De Luca, L. Gioglio, D. Quacci, C. Soldi, The role of proteoglycans in maintaining collagen fibril morphology, Histol. Histopathol. 10 (1995) 583–588.
[50] H.K. Graham, D.F. Holmes, R.B. Watson, K.E. Kadler, Identification of collagen fibril fusion during vertebrate tendon morphogenesis. The process relies on unipolar fibrils and is regulated by collagen–proteoglycan interaction, J. Mol. Biol. 295 (4) (2000) 891–902.
[51] D.E. Birk, E. Zycband, Assembly of the tendon extracellular matrix during development, J. Anat. 184 (1994) 457–463.
[52] G.A. Holzapfel, M. Stadler, T.C. Gasser, Changes in the mechanical environment of stenotic arteries during interaction with stents: computational assessment of parametric stent designs, J. Biomech. Eng. 127 (2005) 166–180.
[53] J. Schröder, P. Wriggers, D. Balzani, A new mixed finite element based on different approximations of the minors of deformation tensors, Comput. Methods Appl. Mech. Engrg. 200 (2011) 3583–3600.
[54] G.A. Holzapfel, G. Sommer, P. Regitnig, Anisotropic mechanical properties of tissue components in human atherosclerotic plaques, J. Biomech. Eng. 126 (2004) 657–665.